Crustal-Scale Disharmonic Structural Pattern of West Junggar: Unveiling a Permian Indentation of Junggar Block Into Northern Kazakhstan Orocline

Yazhou Miao, Jian Zhang, Karel Schulmann, Alexandra Guy, Yingde Jiang, Min Sun, Shuhui Zhang, Sheng Wang

Tectonics®

RESEARCH ARTICLE
10.1029/2022TC007689

Crustal-Scale Disharmonic Structural Pattern of West Junggar: Unveiling a Permian Indentation of Junggar Block Into Northern Kazakhstan Orocline

Yazhou Miao[1,2,3], Jian Zhang[1,2], Karel Schulmann[3,4], Alexandra Guy[3], Yingde Jiang[5], Min Sun[6], Shuhui Zhang[1,2], and Sheng Wang[7]

[1]School of Earth Sciences and Engineering, Sun Yat-Sen University, Guangzhou, China, [2]Southern Marine Science and Engineering Guangdong Laboratory (Zhuhai), Zuhai, China, [3]Center for Lithospheric Research, Czech Geological Survey, Praha 1, Czech Republic, [4]Institut Terre et Environnement de Strasbourg, UMR 7063 Université de Strasbourg—CNRS, Strasbourg, France, [5]State Key Laboratory of Isotope Geochemistry, Guangzhou Institute of Geochemistry, Chinese Academy of Sciences, Guangzhou, China, [6]Department of Earth Sciences, The University of Hong Kong, Pokfulam, Hong Kong, [7]School of Civil Engineering, Anhui Jianzhu University, Hefei, China

Abstract As a crustal-scale orocline in the Central Asian Orogenic Belt (CAOB), the Kazakhstan Orocline in particular its northern limb intervenes the Junggar Block and Chinese Altai. The West Junggar exhibits a structural pattern that is disharmonic from the major structure of the orocline. How and when such a structural complexity was formed remains poorly understood. To address this issue, we carried out detailed mapping, structural analysis and revision of geophysical data in three key areas of the West Junggar. It is shown that different arc chains experienced independent geological histories before they accreted with one another. Such an accretionary process generated the regional D1 deformation in late Carboniferous. Subsequent D2 shortening event produced variable superimposed structures, including crescent-mushroom-like folding in the Boshchekul-Chingiz Arc and partitioned sinistral shearing of the West Karamay Unit. The synformal folding in the Zharma-Saur Arc and crustal-scale Erqis-Zaysan sinistral strike-slip shearing in late Permian—Triassic probably resulted from changing configuration of regional stress. Combined with previous data, we propose that the orogenic fabrics of arc chains and accretionary wedges were primarily related to shaping the basic structural framework of the Kazakhstan Orocline until late Carboniferous. The anticlockwise rotation of the northern limb of the orocline was associated with the indentation of the Junggar Block into the arc chains. Progressive indentation resulted in the first passive bending of arc chains followed by deformation partitioning into simple shear dominated transpression along the western margin of the Junggar Block and pure shear dominated transpression away from the indenter.

Key Points:

- West Junggar exhibits a structural pattern that is disharmonic from the major structure of the northern Kazakhstan Orocline
- Units of West Junggar experienced independent geological and structural histories prior to their mutual accretion in Carboniferous
- Structural complexity of the West Junggar reflects the Junggar Block indented into the northern Kazakhstan Orocline in Permian

Supporting Information:

Supporting Information may be found in the online version of this article.

Correspondence to:

J. Zhang and K. Schulmann,
zhangjian@mail.sysu.edu.cn;
karel.schulmann@geology.cz

Citation:

Miao, Y., Zhang, J., Schulmann, K., Guy, A., Jiang, Y., Sun, M., et al. (2023). Crustal-scale disharmonic structural pattern of West Junggar: Unveiling a Permian indentation of Junggar Block into northern Kazakhstan Orocline. *Tectonics*, *42*, e2022TC007689. https://doi.org/10.1029/2022TC007689

Received 22 NOV 2022
Accepted 24 APR 2023

Author Contributions:

Data curation: Yazhou Miao
Funding acquisition: Jian Zhang, Karel Schulmann, Yingde Jiang
Investigation: Yazhou Miao, Jian Zhang, Shuhui Zhang, Sheng Wang
Writing – original draft: Yazhou Miao
Writing – review & editing: Jian Zhang, Karel Schulmann, Alexandra Guy, Yingde Jiang, Min Sun

1. Introduction

The Central Asian Orogenic Belt (CAOB) is one of the world's largest and geologically complicated Phanerozoic accretionary orogenic belt, characterized by subduction-accretion processes, amalgamation of multiple microcontinents, rotation of blocks, oroclinal bending, associated with intensive deformation and metamorphism (Broussolle et al., 2019; Guy et al., 2020, 2021; Jahn, 2004; Kröner et al., 2010, 2014; Lehmann et al., 2010; Schulmann & Paterson, 2011; Schulmann et al., 2022; Wilhem et al., 2012; Windley et al., 2007; Xiao et al., 2010). Two crustal-scale oroclines, namely the Tuva-Mongol Orocline in the east and the Kazakhstan Orocline in the west, play an important role in shaping the tectonic framework of the CAOB (Xiao et al., 2018; Şengör et al., 1993). In the west, the Kazakhstan Orocline experienced a long-term bending process from Pre-Cambrian to Permian, which was synchronous with the clockwise rotation of the Siberian Craton with respect to the Baltica Craton and the roll-back of different arc chains (Şengör & Natal'in, 1996; P. Li et al., 2018; Xiao et al., 2015; Xiao et al., 2018). In comparison with the southern limb of the orocline that largely strikes NW-SE, the West Junggar in the northern limb exhibits a disharmonic structural pattern that is characterized by an NE-SW-trending belt (Buslov et al., 2004; Hu et al., 2021; Khromykh et al., 2020; Kuibida et al., 2016; P. Li et al., 2018; Figure 1a). So far, the structural complexity of this area has been investigated by some studies in the southern part of the West Junggar, and it was considered to have resulted from oblique subduction driven by oroclinal bending (Choulet et al., 2016; Choulet et al., 2012b), or asymmetric trench retreating (P. Li et al., 2017, 2018). However, previous models did not provide the structural features among the different units in the West Junggar, which hindered

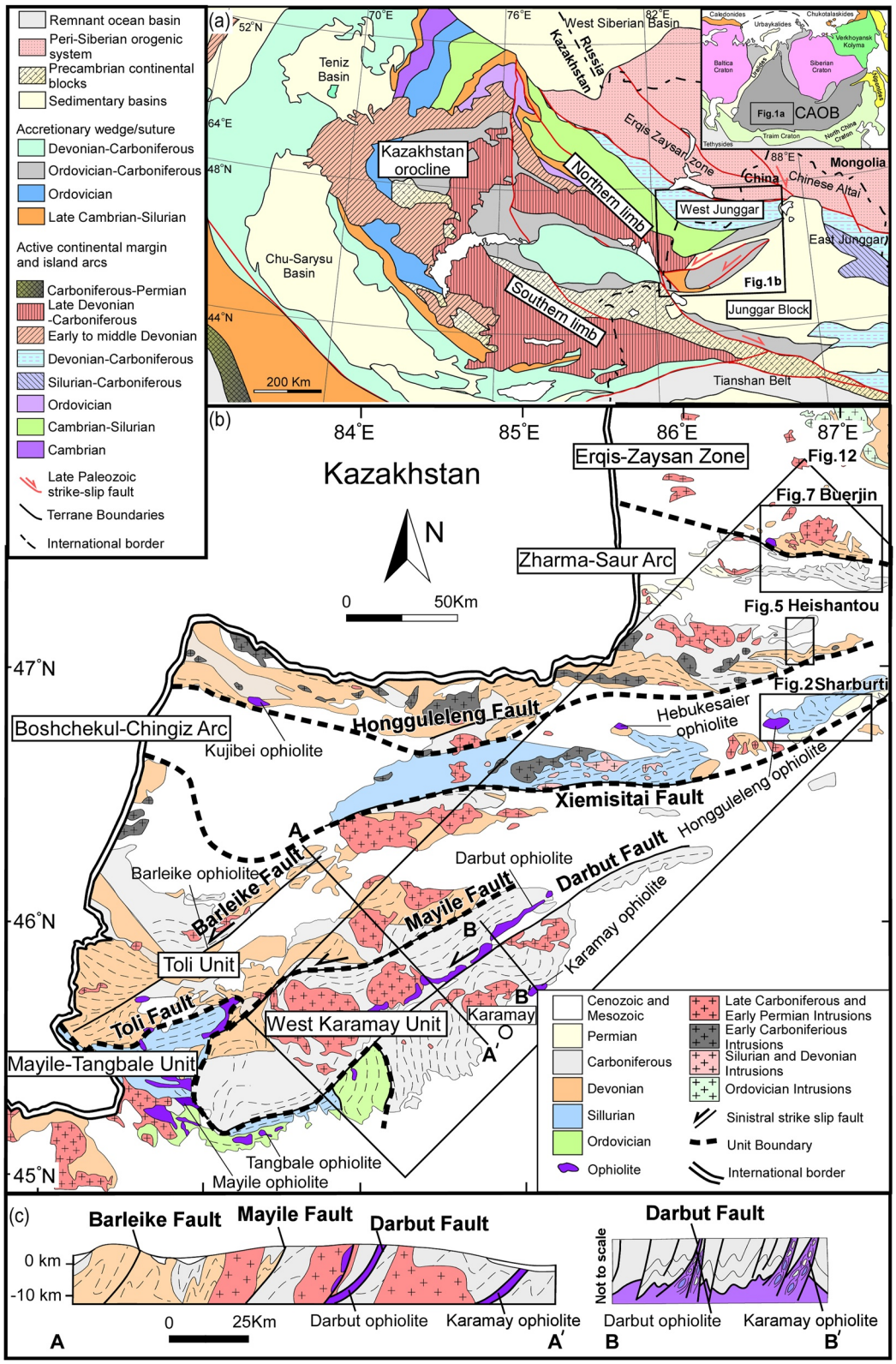

Figure 1.

our understanding of the tectonic process of the orocline formation. It is likely that in addition to the structural evolution related to the oroclinal process, there are deformation structures related to the interaction between the Junggar Block and the Chinese Altai to the north (Figure 1a). However, the detailed structural data from this critical region are absent.

The West Junggar consists of various lithological units of different ages and nature, and variable scales of structures, and thus represents a most promising area to carry out systematic structural and geochronological investigations associated with revision of existing geophysical data. To unveil the structural complexity of the West Junggar, we carried out detailed mapping and structural analysis in the key areas of the Boshchekul-Chingiz Arc, Zharma-Saur Arc, and Erqis-Zaysan Shear Zone, respectively (Figure 1b). With the aid of U-Pb zircon age data, we reconstructed an integrated deformational history for the West Junggar from late Carboniferous to Permian. Combined with available geophysical data, we propose a new model to explain this structural disharmony as a consequence of an indentation of the Junggar Block into the northern Kazakhstan Orocline in Permian.

2. Geological Setting

The eastern part of the Kazakhstan Orocline can be tectonically subdivided into Junggar and north Tianshan lithotectonic units (Soldner et al., 2017; Windley et al., 2002; Xiao et al., 2018; Figure 1a). To the north, the Junggar Block is separated from the Chinese Altai by the NW-trending crustal-scale Erqis-Zaysan shear zone, whereas to the south it is bounded by the Yili Block along the north Tianshan suture zone (Figure 1a). The West Junggar is considered as the area west to the Junggar Block and is subdivided into the southern and northern domains that are separated by the ENE-trending Xiemisitai fault (Feng et al., 1989; B. Liu et al., 2017; Figure 1b).

The southern domain of the West Junggar consists of three lithotectonic units that are tectonically juxtaposed from NW to SE: namely the Toli Unit, the Mayile-Tangbale Unit, and the West Karamay Unit (Figure 1b). The Toli Unit is composed of Devonian to Carboniferous sedimentary series, volcanic rocks and intrusions related to arc magmatism (Choulet et al., 2012a; B. Liu et al., 2016). The Mayile-Tangbale Unit includes late Neoproterozoic to early Silurian ophiolites and Ordovician to Silurian volcanic-sedimentary rocks (B. Liu et al., 2016; Xu et al., 2012, 2013). The West Karamay Unit, located in the southeastern part of the region (Figure 1b), is characterized by a thick and continuous Carboniferous volcaniclastic turbidites that was deposited in a remnant basin setting (Choulet et al., 2012a; Choulet et al., 2016; Choulet et al., 2012b; Yang et al., 2013; P. Zhang et al., 2019, 2018b, 2018c). The Toli Unit is bounded with the Mayile-Tangbale Unit along the Toli fault and is bounded with the West Karamay Unit along the Mayile fault (Figures 1b and 1c). In the southern domain, five ophiolitic mélanges of different ages, namely, the Barleike, Mayile, Tangbale, Darbut, and Karamay mélanges, are mainly distributed along the major tectonic boundaries of the different units (Figure 1b). They are considered to represent the relict of oceanic basins related to the subduction of the Junggar Ocean since early Cambrian (Yang et al., 2012, 2015, 2020).

The northern domain includes two major lithotectonic units, namely the early Paleozoic Boshchekul-Chingiz Arc and late Paleozoic Zharma-Saur Arc, which are separated by the Hongguleleng fault (Yang, Zhao, Zheng, & Xu, 2019; Y. Yang, Zhao, et al., 2020; Figure 1b). The Boshchekul-Chingiz Arc is mainly composed of Ordovician-Silurian arc-related igneous rocks and marine pyroclastic sequences (Choulet et al., 2012a; Choulet et al., 2012c; Yang, Zhao, Xu, et al., 2019; Y. Yang, Zhao, et al., 2020), which were considered to have formed during southward subduction of the Hongguleleng ocean (Song et al., 2020). The Zharma-Saur Arc consists mainly of Devonian to early Carboniferous arc-related igneous and sedimentary rocks (Choulet et al., 2012a; Choulet et al., 2016; Choulet et al., 2012c), which were considered to have formed during southward subduction of the Erqis-Zaysan ocean (Choulet et al., 2016; Windley et al., 2007) or northward subduction of the Hongguleleng ocean (Chen et al., 2017; P. Li et al., 2017; Song et al., 2020; Xiao et al., 2008; Yang et al., 2021; Figure 1b). Junggar Ocean, Erqis-Zaysan Ocean and Hongguleleng Ocean were named by associated ophiolite or the location. The above oceans were located within the wide range of Paleo-Asian Ocean but were separated by different arc chains.

Figure 1. (a) Tectonic map of the Kazakhstan Orocline showing the position of principal arc chains and accretionary wedges (modified after Windley et al. (2007) and Xiao et al. (2018)). Rectangle shows the position of the West Junggar in the Central Asian Orogenic Belt (revised after Xiao et al., 2010). (b) Simplified geological map of the West Junggar showing main lithologies and magmatic bodies of principal tectonic units (revised after Zhang et al. (2018a)). Rectangles show the positions of three studied areas in detail for structures and geochronology. (c) Deep cross section from southern domain of the Western Junggar (A-A′ section modified after J. E. Zhang et al. (2011) and Choulet et al. (2016); B-B' section modified after Zhang et al. (2018b)).

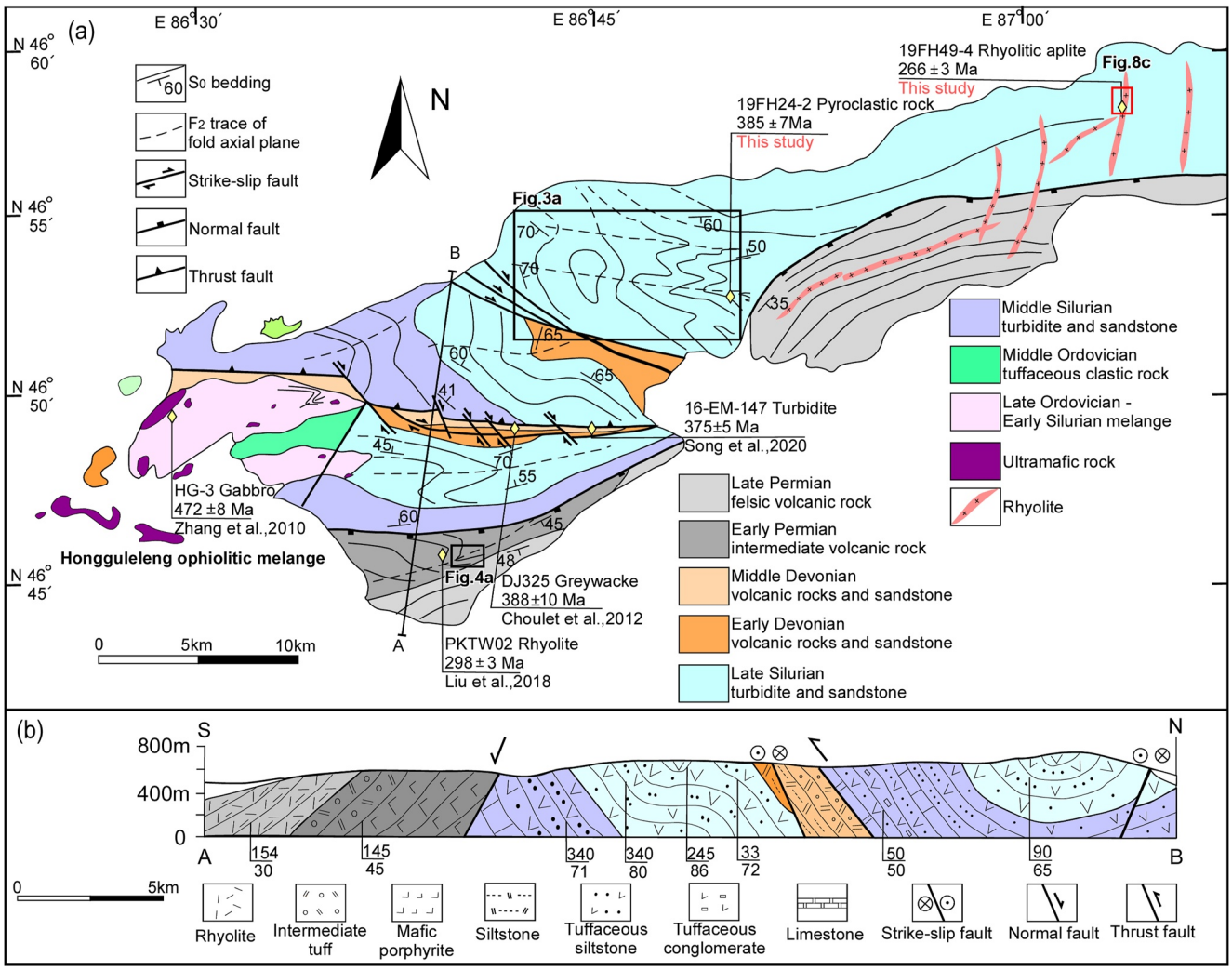

Figure 2. (a) Geological map of the Sharburti area belonging to the eastern extremity of the Boshchekul-Chingiz arc (based on regional 1: 200, 000 geological maps (BGMRX, 1993)). (b) The interpretative cross-section of the Sharburti area showing the main structural features of the studied area.

3. Deformational History of the Northern West Junggar

To constrain the deformational history of the northern West Junggar, we selected three representative areas (i.e., Sharburti area, Heishantou area, and Buerjin area; Figure 1b) in the northern domain and carried out detailed geological mapping together with the structural and geochronological analyses.

3.1. Deformational History of the Sharburti Area

The Sharburti area is located in the northeastern West Junggar and belongs to the Boshchekul-Chingiz Arc (Figures 1b and 2a). It is mainly characterized by the Ordovician-Devonian unit in the northwest and the Permian unit in the southeast (Shen et al., 2013; Figure 2a). The former unit consists of the Middle Ordovician mafic to intermediate volcanic rocks and Silurian-Devonian volcano-sedimentary rocks. The Hongguleleng ophiolitic mélange is located in the western part of the unit and shows tectonic contact with the surrounding rock assemblage. Previous U-Pb dating on the gabbroic dykes of the mélange revealed an age of 472 ± 8 Ma (Y. Zhang & Guo, 2010). The Carboniferous sequence is absent in this area. The latter lithological unit consists of the early Permian volcanic rocks and minor pyroclastic rocks, which are separated from the former unit by a NE-SW-trending fault (G. Liu et al., 2018). Both lithological units were intruded and truncated by a series of nearly N-S-trending rhyolitic aplite dykes giving a U-Pb zircon age of 266 ± 3 Ma (this study, refer to the text below; Figure 2a).

Based on our structural mapping, the Ordovician-Devonian unit experienced two deformational phases, while the Permian unit only records one phase of deformation (Figure 2a). Along the structural profile (Figure 2b), the Ordovician-Devonian unit is characterized by a large-scale composite synformal fold, while the Permian unit is controlled by a normal fault and simply displays a south-dipping trend.

3.1.1. Structures of the Ordovician-Devonian Unit

The central part of the unit preserves the best exposure for deciphering the structural overprinting relationship (Figure 3a). As shown in the structural map, this area displays a crescent-mushroom-like fold interference pattern (Ramsay, 1967; Figure 3a), indicating a superimposition of two phases of deformation. The earlier D1 fabrics are characterized by the nearly N-S-trending and sub-vertically east or west-dipping S0 bedding without penetrative F1 fold axial planar cleavage (Figure 3b). In the western part of the area, the disposition of bedding indicate that it was folded by upright N-S trending F1 folds. The subsequent D2 fabrics are represented by variable scales of F2 folds that mostly plunging to the east at a high angle (Stereonet plots in Figure 3a). They refold the sub-vertical S0 bedding folded by F1 folds and generated a series of E-W-trending upright F2 folds in the eastern part of the study area (Figure 3c).

3.1.2. Structures of the Permian Unit

The Permian unit in the southern part of the study area only experienced the D2 deformation after its deposition. As shown in Figure 4a, the Permian pyroclastic rock layers also exhibit a large-scale symmetric F2 fold. Detailed structural mapping reveals that these F2 fold axes are sub-horizontal that are distinct from steeply plunging F2 folds preserved in the Ordovician-Devonian unit to the north (Figure 4b). Such a structural phenomenon is also evidenced by the fold limbs that are defined by S0 compositional layering without any sign of D1 fabric (Figures 4c and 4d). Structural restoration further constrains that the Permian lithological unit should have deposited after D1 but undergone the subsequent regional D2 deformation.

3.1.3. Restoration of the Superposed Folding Pattern

Considering that the original S0 compositional bedding is well preserved in the Ordovician-Devonian unit, we can utilize the structural symmetry and spatial relations between the D1-D2 structures to restore the approximative deformational history for this area. As shown in the schematic diagram Figure 3d, the F2 folds have E-W trending axial planes and therefore can be interpreted as a result of N-S compression. After restoration along the F2 enveloping surface, the earlier D1 fabrics are mostly characterized by the nearly NWN-SES-trending folds with east steeply dipping axial planes parallel to the regional trend of E-dipping S0 compositional bedding. The Permian unit shows the upright fold that can be correlated to the D2 deformation in the northerly Ordovician-Devonian unit (Figure 4e). However, its axial plane is trending WNW-ESE, which can be interpreted as a result of a nearly NWN-SES-oriented compressional event (Figure 4e). This can indicate that the generalized D2 compression direction affecting all the units in the study area was oriented in the NWN-SES direction.

3.2. Deformational History of the Heishantou Area

The Heishantou area is located in the Zharma-Saur Arc (Figures 1b and 5a). Although the whole area is folded by late large-scale fold, from south to north, it preserves a relatively undisturbed sequence of Middle Devonian to late Carboniferous volcanic and marine sedimentary rocks (Figure 5b). The N-S-trending profile reveals that this area was controlled by open-to-tight upright ENE-WSW-trending F1 folds, which folded the original S0 compositional layering (Figure 5b). Our detailed mapping also reveals that numerous sills and dykes are intruded into the volcano-sedimentary rocks (Figures 5a and 5b). The only known age of these dykes was a 338 ± 1 Ma rhyolitic aplite sill reported by P. Li et al. (2017). Therefore, in this study, we also dated three sills and dykes from different structural locations, to better constrain the timing of regional deformation.

We mapped out the key structural elements for the area that is characterized by a large-scale synformal fold F2, which refolded the upright F1 folds in the southern part of the study area (Figure 6a). Due to the strain heterogeneity in the different parts of the large-scale fold F2, from the south to the north of the Heishantou area was gradually unaffected by the D2 deformation (Figure 6a). Regionally, the F2 fold hinge steeply plunges to the NWN. The fold exhibits slightly asymmetrical geometry with straight limbs and a sharp hinge. Both fold limbs are mainly composed of turbidites which are characterized by alternating high-competence sandstones and low-competence shales (Figures 6b and 6c). As shown in Figure 6a, the F2 fold axial plane largely represents

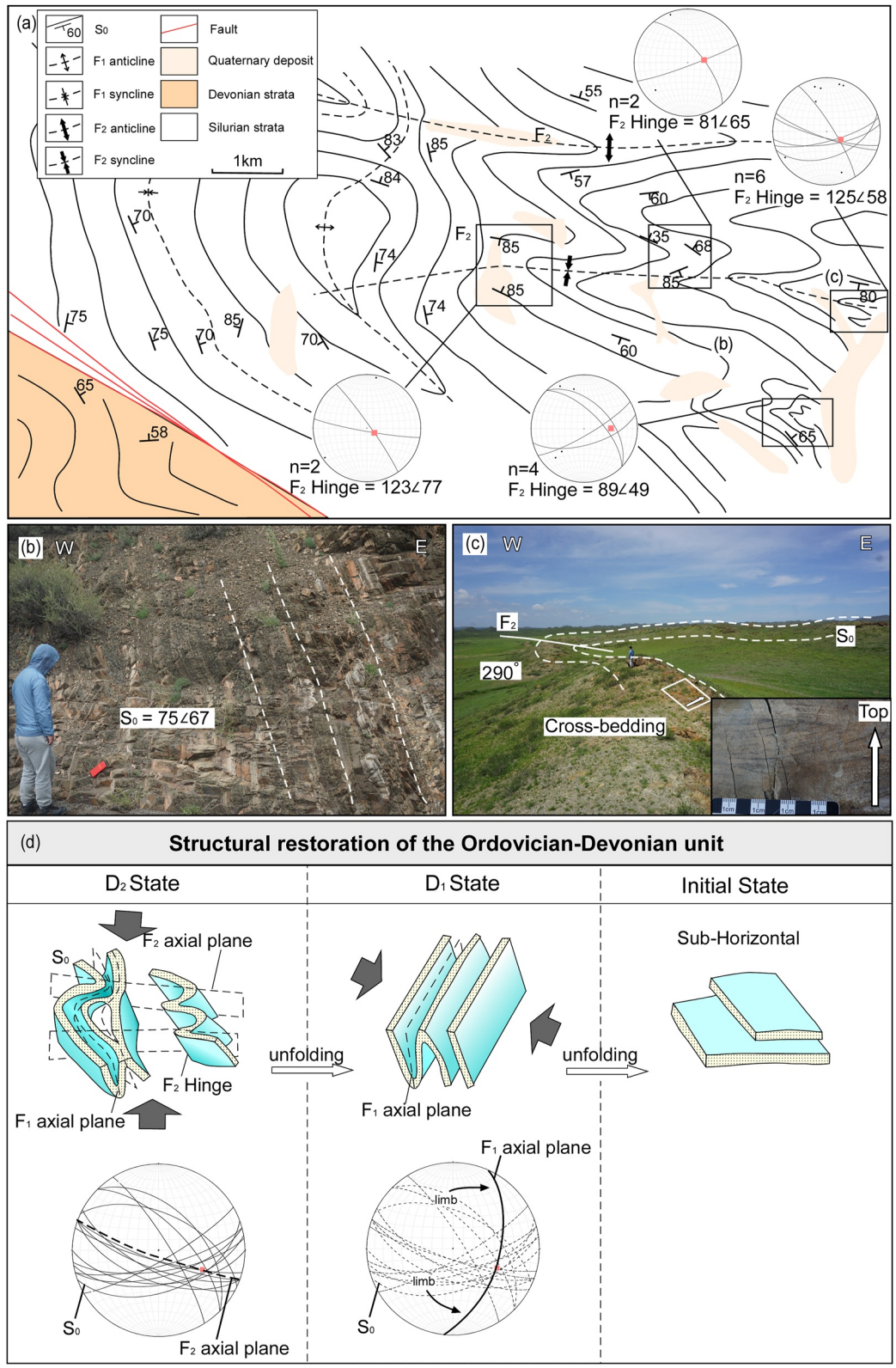

Figure 3. (a) Structural map of the Ordovician-Devonian unit in the Sharburti area. (b) Field photograph of nearly N-S-trending and sub-vertical S0 bedding. (c) F2 fold deforming the earlier S0 bedding. E-W-trending sub-vertical F2 fold axial plane is shown. Lower left inset shows the cross-bedding feature allowing to restore the position of bedding. (d) Structural restoration of the Ordovician-Devonian unit from the initial state via D1 folding to finite D2 strain pattern.

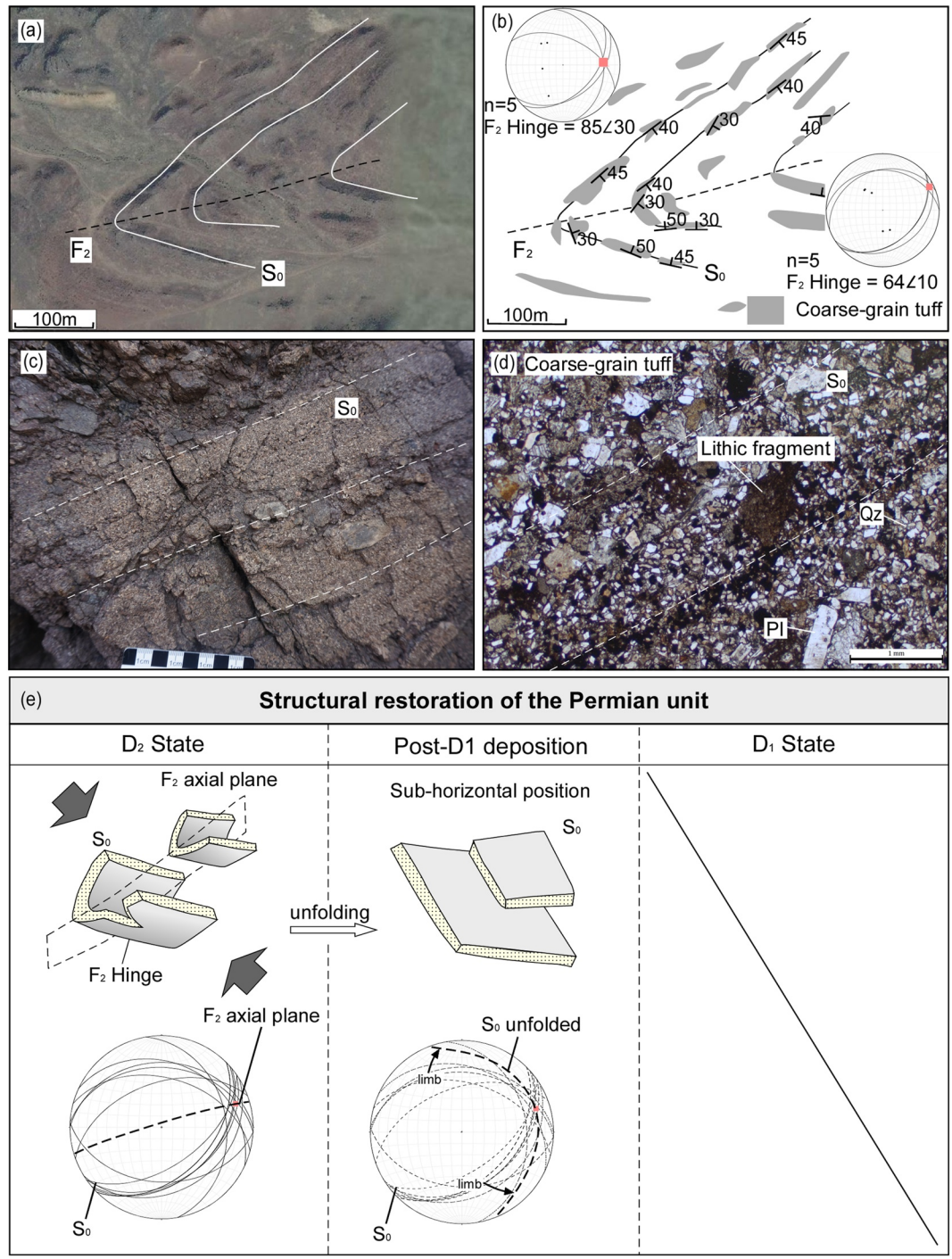

Figure 4. (a) Satellite image of the Permian unit showing the distribution of S0 and typical F2 folds. (b) Structural map of the Permian unit with the reconstructed axial plane. (c) Field photograph of bedding of tuffs. (d) Micro-photograph showing the texture of coarse-grained crystal tuff. (e) Structural restoration of the Permian unit. The mineral abbreviations are used in this manuscript are after Whitney and Evans (2010). Qz: Quartz; Pl: Plagioclase.

the bisector of an inter-limb angle, which leads us to approximately infer the D2 deformation as the consequence of a nearly ENE-WSW-oriented shortening (Figure 6d). After restoration, the earlier D1 fabrics become nearly E-W-trending and sub-vertically N-dipping S0 compositional beddings (Figure 6d). They most likely resulted from an approximately N-S-oriented shortening during the D1 deformation, which is consistent with the structural profile showing that the northern zone unaffected by the D2 deformation still preserves the E-W-trending

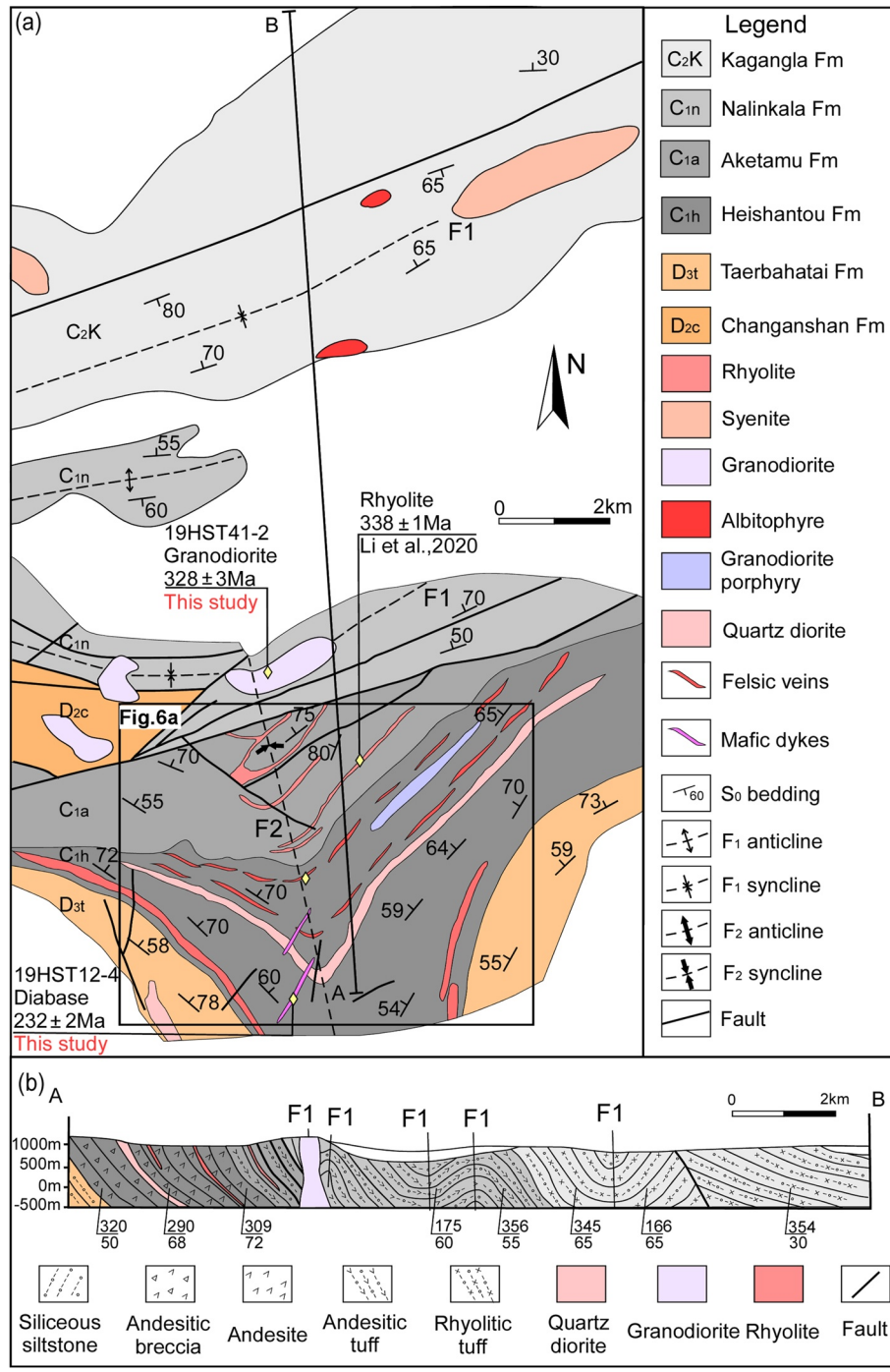

Figure 5. (a) Geological map of the Heishantou area (based on regional 1: 200, 000 geological maps (BGMRX, 1993)) with positions of dated samples. (b) Schematic cross-section of the Heishantou area showing the main D1 structural pattern.

F1 upright folds (Figure 5b). The overall structural features indicate that both D1-D2 deformations in this area should have occurred after the deposition of the Carboniferous volcanic clastic and marine sediments (Figure 6d).

3.3. Deformational History of the Buerjin Area

The Buerjin area covers lithological units from the northern Zharma-Saur Arc and southern Erqis-Zaysan zone, both of which are reworked by a branch of the crustal-scale sinistral Erqis fault zone (P. Li et al., 2017; C. L.

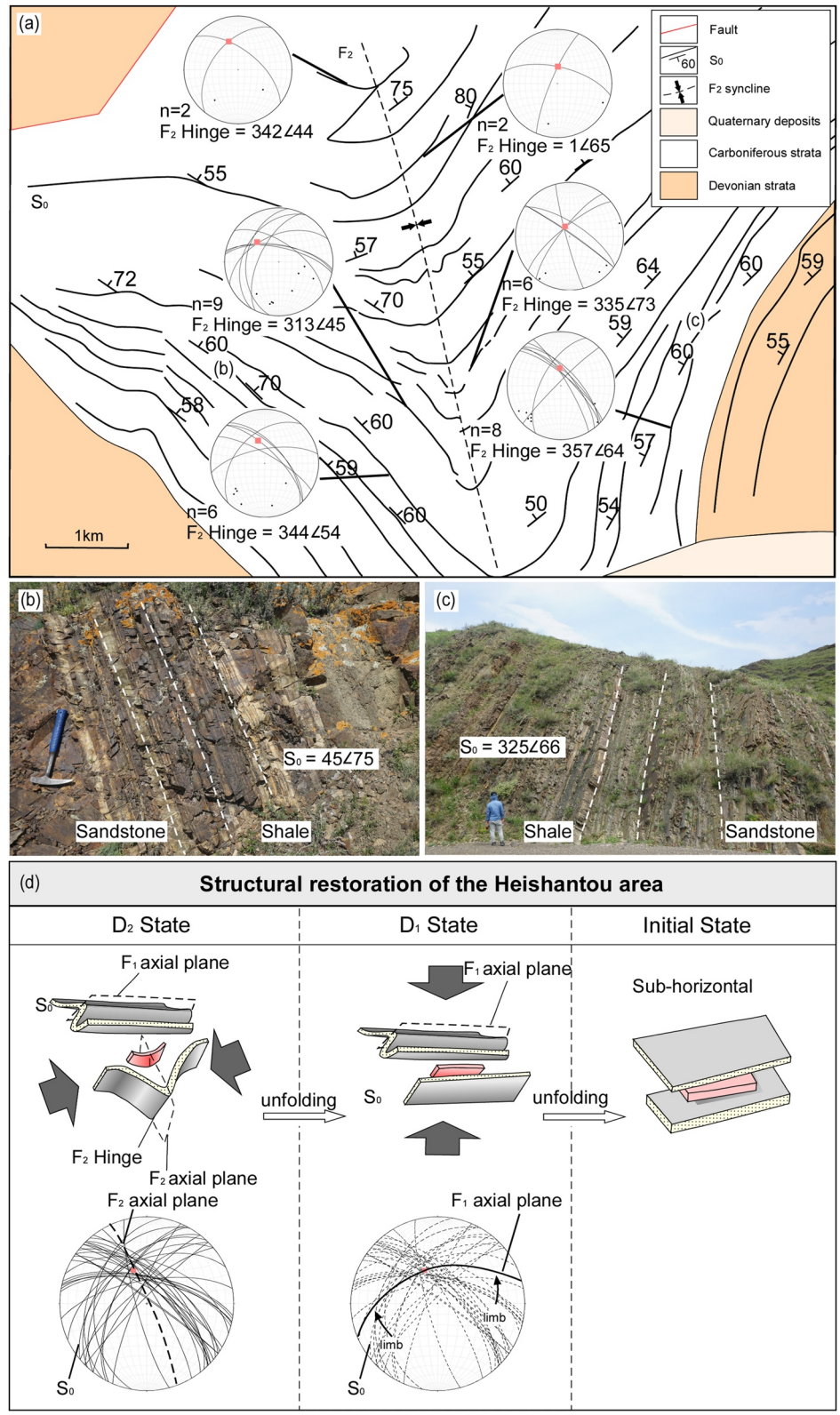

Figure 6. (a) Structural map of the Heishantou area, with reconstructed axial plane and Stereonets used for reconstruction of the fold. (b and c) Photographs of turbidites which are characterized by the alternation of sandstone and shale beds. (d) Structural restoration of the Heishantou area from its original state via D1 folding to D2 chevron folding.

Zhang et al., 2012; Figure 1b). The northern Zharma-Saur Arc is composed of Carboniferous interlayered turbidites and volcanoclastic rocks with minor limestone, whereas the Erqis-Zaysan zone is dominated by the Devonian marine sediments that show affinity to the Chinese Altai (P. Li et al., 2017; Figure 7a). The two structural profiles reveal that the two units both experienced earlier F1 folding and subsequent D2 shearing deformations (Figure 7b). Regional F1 folds are mainly characterized by the sub-vertical S0 bedding, whereas the late D2 shearing is mainly localized along the contact between the two units (Figures 7c and 7d). Numerous pre- and post-tectonic magmatic plutons of this region largely bracket the timing of deformation of 300-268 Ma (Tong et al., 2014; Wang et al., 2012; Figure 7a). The structural restoration indicates that prior to the D2 shearing, both units underwent a similar NEN-SWS-oriented compressional deformation D1 that produced of upright F1 folds of variable size (Figure 7e).

4. Magnetic and Gravity Analysis of the West Junggar Crustal Structures

In order to better constrain the principal orientation of tectonic units and their internal structuration we evaluated the existing magnetic and gravity data. The analysis of potential field data is a powerful but underused tool for the structural analysis of orogenic fabrics previously applied in neighboring regions (Guy et al., 2020, 2021). Magnetic and gravity signals characterize the crustal structures revealed by the magnetic susceptibility and density contrasts as suitable filtering procedures enhance the anomalies at different crustal levels. The magnetic and gravity lineaments were identified with the tilt angle (Miller & Singh, 1994; Verduzco et al., 2004), which highlights the orientation of the tectonic fabrics of the basement, and the multiscale edge analysis (Archibald et al., 1999; Holden et al., 2000; Hornby et al., 1999; Vallée et al., 2004), which provides the strikes and dips of these anomalies. The quantification of these geophysical anomaly trends and their relationships to lithologies and tectonic units help to determine the possible deep-seated geological structures of the West Junggar (details about the methodology, e.g., Guy et al., 2020 and references therein).

4.1. Magnetic and Gravity Anomaly Maps

The magnetic anomaly map, proceeding from the Earth Magnetic Anomaly Grid available at a spatial resolution of 2×2 arc min (Maus et al., 2009), displays anomalies ranging from −290 to 290 nT. It reveals magnetic highs for the Zharma-Saur and the Boshchekul-Chingiz Arcs, for the northern part of the Toli Unit, and partly for the Junggar Block (Figures 8a and 8b). In general, the ophiolitic mélanges correspond with moderate magnetic highs, except for the Darbut, Karamay and Kujibei ophiolites, which correlate with intermediate magnetic signals. The NE–SW-trending transpressive zone from south of the Barleike Fault to the Junggar Block (Choulet et al., 2016; Choulet et al., 2012b) correlate with intermediate magnetic signals (Figure 8c).

The Bouguer gravity anomaly map, proceeding from the Earth Global Model 08 available at a spatial resolution of 2.5×2.5 arc min and obtained using the standard mean crustal density of 2,670 kg/m^3 (Pavlis et al., 2012), shows anomalies ranging from −195 to −90 mGal. It reveals two prominent gravity highs: in the central part of the Zharma-Saur Arc and at the western boundary of the Junggar Block, along the Darbut Fault (Figure 8d). The Boshchekul-Chingiz Arc rather corresponds to an intermediate gravity signal (Figure 8d). In general, the ophiolitic mélanges also correlate with intermediate gravity signals. The gravity low in the central part of the Toli Unit extends to the NE and the SW, although partly concealed by the gravity high along the Darbut Fault (Figure 8d).

Except for the Darbut Fault, the Erqis, Hongguleleng, Xiemisitai, Barleike and Mayile faults do not have strong magnetic and gravity signatures (Figures 8c and 8d). The Junggar Block presents a low frequency and low amplitude magnetic high matching with large-scale low gravity signatures.

4.2. Tilt Angle—Geophysical Mapping of the Main Structural Fabrics

The tilt angle method was performed on both magnetic and gravity anomalies and the extraction of lineaments can be correlated with the main tectonic fabrics of the basement. It reveals three groups of magnetic and gravity anomaly trends (Figures 8c and 8d): (a) the NW–SE-trending lineaments, mostly located in Kazakhstan, are subparallel to the northern limb of the Kazakhstan Orocline; (b) the ENE–WSW lineaments correspond to the main orientation of the Zharma-Saur and Boshchekul-Chingiz Arcs, and the western part of the Toli Unit; (c) the NE–SW-trending lineaments are mainly located at the western boundary of the Junggar Block. The Junggar Block displays all three groups of lineaments roughly equally.

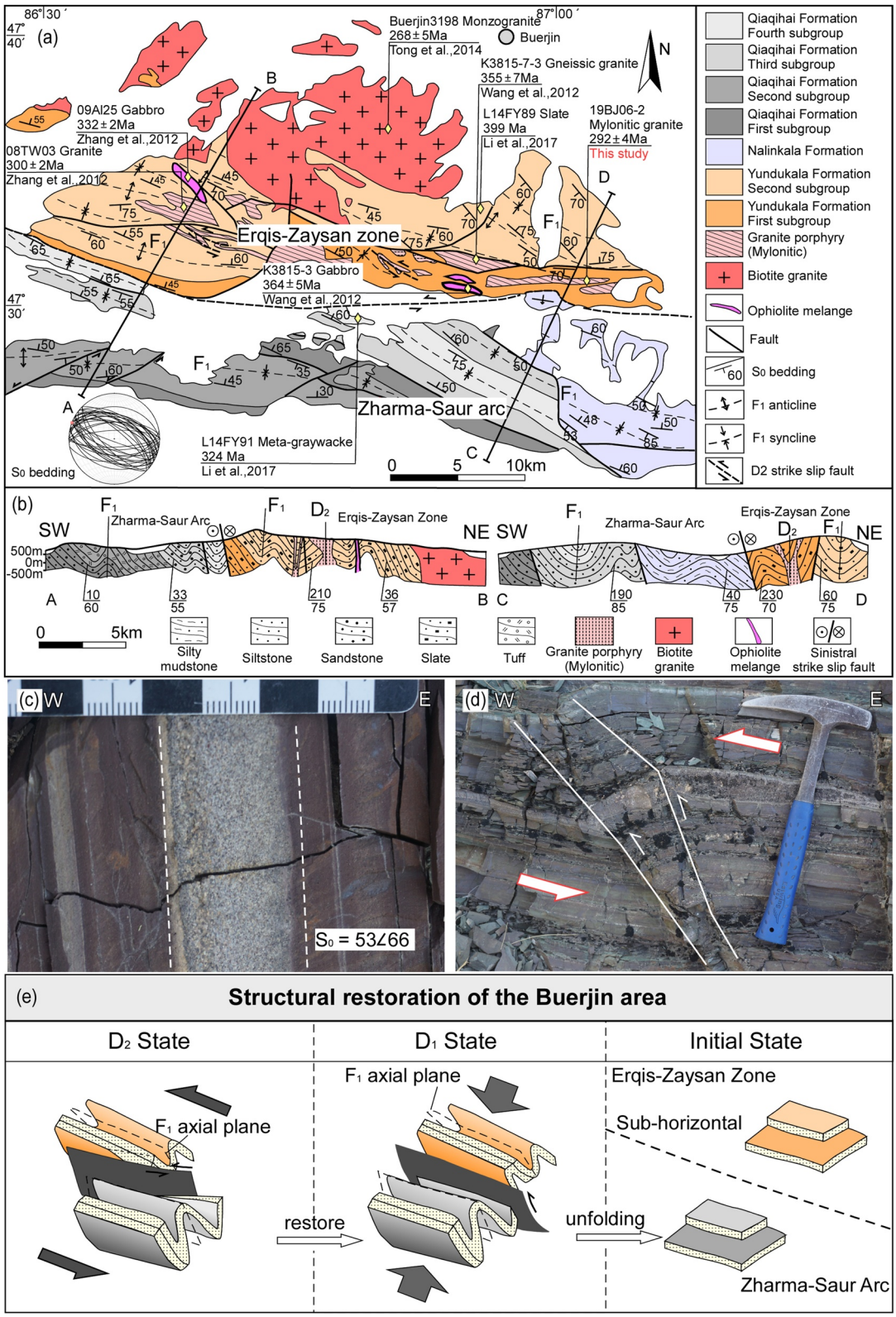

Figure 7. (a) Geological map of the Buerjin area (based on regional 1: 200, 000 geological maps (BGMRX, 1993)). Permian granite in the NW corner of the map is post-tectonic. (b) The interpretative cross-section of the Buerjin area showing mainly F1 folding of Devonian and Carboniferous bedding as well as Carboniferous granite sheets. (c) Sub-vertical S0 bedding. (d) The S0 is affected by D2 shearing. (e) Structural restoration of the Buerjin area from initial sub-horizontal bedding position via F1 folding to late-sinistral faulting (modified from Li et al. (2017)).

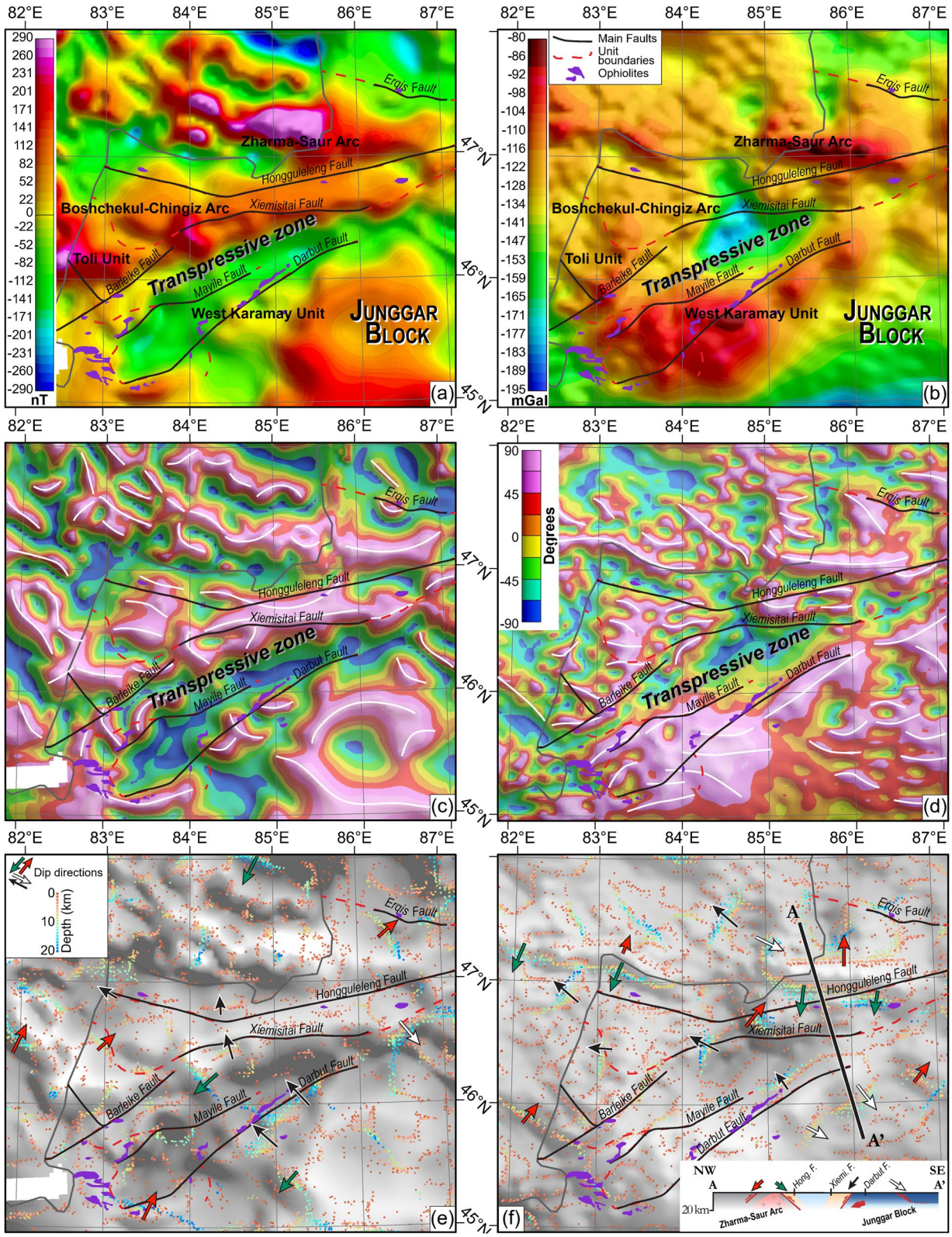

Figure 8.

4.3. Multiscale Edge Analysis—Distribution and Orientation of the Main Tectonic Contacts

Multiscale edge detection is processed for the analytic signal of magnetic anomalies and for the Bouguer gravity anomalies for 20 upward continuations from 0 to 40 km, providing information about the locations and dips of substantial magnetic and gravity contrasts. The results display the main geological contacts from 0 to 20 km depth (Figures 8e and 8f). For both magnetic and gravity analysis, the string orientations of maxima mostly correspond to the strikes of the lineaments obtained with the tilt angle techniques. Regarding the distribution of the dips of these contacts, the magnetic and the gravity multiscale edge results reveal NW-dipping contacts (black arrows in Figures 8e and 8f), which are equally distributed in the West Junggar on the magnetic and gravity maps. Similarly, the few deep SE-dipping contacts (white arrows) seem to be restricted to the Junggar Block both on the magnetic and gravity maps. Major NE-dipping geological contacts are also observed on both magnetic and gravity results with a pronounced NEN-SWS pairing of dips observed along the Zharma-Saur Arc in the gravity map (red and green arrows in Figures 8e and 8f, respectively). The inclination of each contact and its continuity in depth are determined by the distribution of the maxima points on the map versus the resulting depths obtained by the multi-scale edge technics as exemplified by the schematic profile in Figure 8f.

5. Zircon U-Pb Geochronology

To constrain the time range of the D1-D2 deformation events, we collected six representative samples of different rock types from the above three areas and utilized LA-ICP-MS to carry out U-Pb zircon age dating. The sample age results are listed in Table 1.

5.1. Sharburti Area: Pre-D1 Sample 19FH24-2 and Post-D2 Sample 19FH49-4

Sample 19FH24-2 was collected from the pyroclastic rock layers in the northern Ordovician-Devonian unit (Figure 2a). In the field, the pyroclastic rocks are characterized by the sub-vertical S0 bedding, which is folded by the hundred-meter-scale steeply plunging fold F2 (Figure 9a). In the thin section, the sample mainly contains quartz and plagioclase fragments up to 0.1 mm in size and minor fine-grained volcanic glass (Figure 10a). Zircon grains extracted from Sample 19FH24-2 are mostly prismatic and euhedral in shape, and range 60–150 μm in length with an aspect ratio of 2:1–3:1 (Figure 11a). These zircon grains show typical oscillatory zoning in their CL images and have Th/U ratios of 0.44–1.14 (Table 1), suggesting a magmatic origin (Figure 11a). A total of 25 analyses were conducted on different grains and five of them yielded a cluster with a weighted mean $^{206}Pb/^{238}U$ age of 385 ± 7 Ma (MSWD = 0.23; Figure 12a). In our interpretation, this age represents the crystallization age of the rock that pre-dated the regional D1 deformation.

Sample 19FH49-4 was collected from the nearly N-S-trending rhyolitic aplite dykes in the northern Ordovician-Devonian lithological unit (Figure 2a). Although these dykes are slightly folded, they intruded and truncated both regional D1 and D2 structures affecting -turbidite (Figure 9b). A detailed map indicates that the curvature of the aplite dykes is the consequence of the later dextral fault and postdating F2 folding (Figure 9c). In the thin section, the sample contains fine-grained quartz and plagioclase up to 0.5 mm in size (Figure 10b). Zircon grains show euhedral crystal shapes and 100–200 μm in length with an aspect ratio of 2:1–3:1 (Figure 11b). CL images show that the zircon grains have typical magmatic oscillatory zones (Figure 11b), which is consistent with the Th/U ratios of 0.57–1.17 (Table 1). Twenty-five analyses on these zircon grains yielded a $^{206}Pb/^{238}U$ weighted mean age of 266 ± 3 Ma (MSWD = 1.6; Figure 12b). The N-S trending rhyolite dykes are often perpendicular to axial planes of F2 folds and therefore can be interpreted as related to F2 folding. Thus, the zircon age of the dyke also marks the minimum time constraints on the regional D2 deformation.

Figure 8. Major crustal structures constrained by magnetic and gravity signal analyses. The boundaries of the different units, the principal faults and the ophiolites described in this study are superimposed on each map. (a) Magnetic map extracted from the Earth Magnetic Anomaly Grid available at a spatial resolution of 2 × 2 arc min. (b) Bouguer gravity anomaly map extracted from the Earth Global Model 08 available at a spatial resolution of 2.5 × 2.5 arc min. (c) Tilt angle of the magnetic anomalies and the main lineaments (white lines). (d) Tilt angle of the gravity anomalies and the main lineaments (white lines). (e) Multiscale edge analysis from the surface to 20 km depth of the analytic signal results computed from the magnetic anomaly map in gray scale. (f) Multiscale edge analysis from the surface to 20 km depth of the gravity results computed from the Bouguer gravity map. Inset shows the schematic profile A-A′ that displays the dip of the main tectonic contacts (inclined red lines) from the Zharma-Saur Arc to the Junggar Block.

Table 1
U-Pb Data of Zircon (With 1σ Error) for Samples 19FH24-2, 19FH49-4, 19HST41-2, 19HST12-4, and 19BJ06-2

	Th/U	Pb^{207}/Pb^{206}		Pb^{207}/U^{235}		Pb^{206}/U^{238}		Pb^{207}/Pb^{206}		Pb^{207}/U^{235}		Pb^{206}/U^{238}		
Sample spot no	Ratios	Ratios	1σ	Ratios	1σ	Ratios	1σ	Ages (Ma)	1σ	Ages (Ma)	1σ	Ages (Ma)	1σ	Concordant (%)
19FH24-2 Pyroclastic rock														
1	0.42	0.0546	0.0014	0.4734	0.0125	0.0630	0.0014	394	55	394	9	394	8	100
2	0.45	0.0553	0.0017	0.5209	0.0165	0.0684	0.0015	424	67	426	11	426	9	100
3	1.14	0.0560	0.0017	0.5536	0.0173	0.0718	0.0016	450	66	447	11	447	10	100
4	0.07	0.0553	0.0013	0.5268	0.0132	0.0691	0.0015	425	51	430	9	431	9	100
5	0.66	0.0562	0.0017	0.5779	0.0184	0.0746	0.0017	461	67	463	12	464	10	100
6	0.79	0.0566	0.0021	0.5076	0.0191	0.0651	0.0015	475	81	417	13	407	9	97
7	0.44	0.0553	0.0014	0.5215	0.0141	0.0685	0.0015	422	56	426	9	427	9	100
8	0.80	0.0568	0.0020	0.4926	0.0175	0.0630	0.0014	482	76	407	12	394	9	97
9	0.63	0.0572	0.0016	0.5044	0.0144	0.0640	0.0014	498	60	415	10	400	9	96
10	1.05	0.0561	0.0016	0.5011	0.0146	0.0649	0.0014	455	61	413	10	405	9	98
11	0.87	0.0561	0.0015	0.4997	0.0140	0.0647	0.0014	455	59	412	9	404	9	98
12	0.60	0.0566	0.0017	0.5228	0.0160	0.0671	0.0015	475	65	427	11	419	9	98
13	0.56	0.0552	0.0025	0.5287	0.0238	0.0695	0.0016	420	97	431	16	433	10	101
14	0.91	0.0561	0.0013	0.5001	0.0123	0.0647	0.0014	456	51	412	8	404	9	98
15	0.62	0.0575	0.0022	0.4916	0.0190	0.0621	0.0014	510	82	406	13	388	9	95
16	1.02	0.0574	0.0016	0.5133	0.0151	0.0650	0.0014	506	62	421	10	406	9	96
17	0.58	0.0564	0.0017	0.5060	0.0159	0.0651	0.0014	468	67	416	11	407	9	98
18	0.57	0.0566	0.0018	0.5644	0.0180	0.0724	0.0016	477	68	454	12	450	10	99
19	0.69	0.0548	0.0014	0.4596	0.0119	0.0609	0.0013	405	54	384	8	381	8	99
20	0.60	0.0567	0.0014	0.5283	0.0139	0.0676	0.0015	481	55	431	9	422	9	98
21	0.51	0.0567	0.0015	0.5166	0.0139	0.0663	0.0014	477	56	423	9	414	9	98
22	0.88	0.0558	0.0015	0.5152	0.0139	0.0671	0.0015	443	57	422	9	419	9	99
23	0.92	0.0563	0.0015	0.5444	0.0146	0.0703	0.0015	463	57	441	10	438	9	99
24	0.69	0.0571	0.0014	0.4656	0.0118	0.0592	0.0013	495	53	388	8	371	8	95
19FH49-4 Rhyolitic aplite														
1	0.73	0.0516	0.0013	0.3040	0.0081	0.0428	0.0009	268	58	270	6	270	6	100
2	0.93	0.0528	0.0014	0.2943	0.0083	0.0405	0.0009	320	60	262	7	256	5	98
3	1.10	0.0537	0.0013	0.2952	0.0077	0.0399	0.0009	357	55	263	6	252	5	96
4	0.96	0.0529	0.0014	0.3060	0.0083	0.0420	0.0009	323	58	271	6	265	6	98
5	0.73	0.0540	0.0021	0.3142	0.0122	0.0423	0.0010	370	84	277	9	267	6	96
6	1.08	0.0526	0.0012	0.3116	0.0077	0.0430	0.0009	311	53	275	6	272	6	99
7	0.57	0.0521	0.0014	0.2959	0.0083	0.0412	0.0009	289	60	263	6	261	6	99
8	0.58	0.0540	0.0017	0.3213	0.0106	0.0432	0.0010	369	71	283	8	273	6	96
9	0.80	0.0521	0.0015	0.3006	0.0089	0.0419	0.0009	289	64	267	7	264	6	99
10	0.58	0.0543	0.0013	0.3074	0.0079	0.0411	0.0009	383	54	272	6	260	5	95
11	0.59	0.0522	0.0017	0.2979	0.0101	0.0414	0.0009	296	74	265	8	261	6	99
12	1.04	0.0524	0.0014	0.3059	0.0083	0.0424	0.0009	301	59	271	6	268	6	99
13	0.83	0.0519	0.0014	0.2882	0.0078	0.0403	0.0009	280	59	257	6	255	5	99
14	0.95	0.0584	0.0015	0.3396	0.0089	0.0422	0.0009	543	54	297	7	267	6	89
15	0.70	0.0561	0.0014	0.3219	0.0081	0.0416	0.0009	456	53	283	6	263	5	92
16	1.03	0.0561	0.0016	0.3346	0.0097	0.0432	0.0009	457	62	293	7	273	6	93

Table 1
Continued

Sample spot no	Th/U	Pb^{207}/Pb^{206}		Pb^{207}/U^{235}		Pb^{206}/U^{238}		Pb^{207}/Pb^{206}		Pb^{207}/U^{235}		Pb^{206}/U^{238}		
	Ratios	Ratios	1σ	Ratios	1σ	Ratios	1σ	Ages (Ma)	1σ	Ages (Ma)	1σ	Ages (Ma)	1σ	Concordant (%)
17	1.02	0.0547	0.0015	0.3062	0.0085	0.0406	0.0009	398	59	271	7	257	5	94
18	1.14	0.0522	0.0013	0.3098	0.0078	0.0430	0.0009	295	55	274	6	272	6	99
19	1.17	0.0548	0.0013	0.3282	0.0082	0.0435	0.0009	404	53	288	6	274	6	95
20	0.62	0.0512	0.0013	0.3007	0.0076	0.0426	0.0009	250	56	267	6	269	6	101
21	0.74	0.0521	0.0015	0.3001	0.0085	0.0418	0.0009	290	63	267	7	264	5	99
22	1.14	0.0561	0.0017	0.3329	0.0100	0.0430	0.0009	456	65	292	8	272	6	93
23	1.17	0.0532	0.0013	0.3267	0.0082	0.0446	0.0009	336	55	287	6	281	6	98
24	0.64	0.0518	0.0016	0.2995	0.0094	0.0419	0.0009	278	70	266	7	265	5	100
25	0.83	0.0539	0.0018	0.3240	0.0111	0.0436	0.0009	366	75	285	9	275	6	96
19HST41-2 Granodiorite														
1	0.61	0.0527	0.0026	0.3461	0.0164	0.0478	0.0009	315	107	302	12	301	6	100
2	0.56	0.0531	0.0035	0.3858	0.0251	0.0528	0.0010	332	143	331	18	332	6	100
3	0.54	0.0528	0.0025	0.3862	0.0174	0.0531	0.0010	321	103	332	13	334	6	101
4	0.68	0.0535	0.0027	0.3912	0.0189	0.0532	0.0010	350	109	335	14	334	6	100
5	0.48	0.0536	0.0025	0.3846	0.0175	0.0522	0.0010	354	102	330	13	328	6	99
6	0.58	0.0513	0.0049	0.3670	0.0351	0.0520	0.0010	253	207	318	26	327	6	103
7	0.54	0.0517	0.0048	0.3749	0.0343	0.0527	0.0011	273	198	323	25	331	6	102
8	0.74	0.0518	0.0021	0.3717	0.0146	0.0521	0.0010	277	90	321	11	328	6	102
9	0.80	0.0523	0.0021	0.3621	0.0143	0.0503	0.0009	300	90	314	11	316	6	101
10	0.56	0.0535	0.0051	0.3879	0.0369	0.0527	0.0010	351	203	333	27	331	6	99
11	0.70	0.0531	0.0019	0.3763	0.0130	0.0515	0.0009	331	80	324	10	324	6	100
12	0.50	0.0528	0.0027	0.3770	0.0186	0.0519	0.0010	319	110	325	14	326	6	100
13	0.70	0.0530	0.0017	0.3800	0.0116	0.0521	0.0009	328	72	327	9	327	6	100
14	0.52	0.0538	0.0020	0.3901	0.0142	0.0527	0.0010	363	83	335	10	331	6	99
15	0.76	0.0529	0.0024	0.3866	0.0172	0.0531	0.0010	322	101	332	13	334	6	101
16	0.72	0.0535	0.0026	0.3892	0.0181	0.0528	0.0010	350	104	334	13	332	6	99
17	0.58	0.0538	0.0030	0.3816	0.0206	0.0515	0.0010	362	119	328	15	324	6	99
18	0.48	0.0541	0.0018	0.3793	0.0123	0.0509	0.0009	375	75	327	9	320	6	98
19	0.53	0.0526	0.0019	0.3707	0.0126	0.0512	0.0009	311	79	320	9	322	6	101
20	0.53	0.0538	0.0029	0.4001	0.0212	0.0540	0.0010	363	117	342	15	339	6	99
21	0.80	0.0527	0.0023	0.3775	0.0163	0.0520	0.0010	316	98	325	12	327	6	100
22	0.61	0.0531	0.0027	0.3864	0.0192	0.0528	0.0010	333	111	332	14	332	6	100
23	0.62	0.0527	0.0024	0.3843	0.0172	0.0529	0.0010	317	101	330	13	332	6	101
24	0.55	0.0525	0.0021	0.3787	0.0145	0.0524	0.0010	305	88	326	11	329	6	101
19HST12-4 Diabase														
1	0.23	0.0517	0.0025	0.2613	0.0128	0.0367	0.0008	273	108	236	10	232	5	98
2	0.29	0.0506	0.0013	0.2557	0.0065	0.0367	0.0008	224	57	231	5	232	5	100
3	0.10	0.0509	0.0040	0.2579	0.0203	0.0368	0.0009	238	173	233	16	233	5	100
4	0.17	0.0510	0.0011	0.2577	0.0056	0.0367	0.0008	240	47	233	4	232	5	100
5	0.40	0.0535	0.0012	0.2701	0.0064	0.0367	0.0008	349	51	243	5	232	5	95
6	0.30	0.0511	0.0016	0.2569	0.0080	0.0365	0.0008	245	70	232	6	231	5	100
7	0.53	0.0524	0.0022	0.2607	0.0107	0.0361	0.0008	303	92	235	9	229	5	97

Table 1
Continued

Sample spot no	Th/U Ratios	Pb^{207}/Pb^{206} Ratios	1σ	Pb^{207}/U^{235} Ratios	1σ	Pb^{206}/U^{238} Ratios	1σ	Pb^{207}/Pb^{206} Ages (Ma)	1σ	Pb^{207}/U^{235} Ages (Ma)	1σ	Pb^{206}/U^{238} Ages (Ma)	1σ	Concordant (%)
8	0.27	0.0512	0.0018	0.2576	0.0091	0.0365	0.0008	250	79	233	7	231	5	99
9	0.29	0.0523	0.0026	0.2647	0.0129	0.0368	0.0008	296	108	239	10	233	5	98
10	0.41	0.0528	0.0023	0.2667	0.0118	0.0367	0.0008	321	97	240	9	232	5	97
11	0.14	0.0525	0.0012	0.2655	0.0061	0.0367	0.0008	306	51	239	5	233	5	97
12	0.28	0.0530	0.0012	0.2686	0.0059	0.0368	0.0008	330	48	242	5	233	5	96
13	0.23	0.0531	0.0012	0.2685	0.0059	0.0367	0.0008	334	48	242	5	232	5	96
14	0.77	0.0539	0.0014	0.2726	0.0072	0.0367	0.0008	367	58	245	6	232	5	95
15	0.41	0.0519	0.0016	0.2630	0.0083	0.0368	0.0008	283	70	237	7	233	5	98
16	0.15	0.0493	0.0011	0.2495	0.0056	0.0368	0.0008	160	52	226	5	233	5	103
17	0.33	0.0524	0.0016	0.2648	0.0080	0.0367	0.0008	304	67	239	6	232	5	97
18	0.28	0.0515	0.0017	0.2604	0.0084	0.0367	0.0008	264	73	235	7	232	5	99
19	0.52	0.0500	0.0012	0.2533	0.0062	0.0368	0.0007	197	56	229	5	233	5	101
20	0.53	0.0506	0.0020	0.2561	0.0100	0.0367	0.0008	223	89	232	8	233	5	100
21	0.45	0.0502	0.0022	0.2534	0.0110	0.0367	0.0007	203	98	229	9	232	5	101
22	0.38	0.0513	0.0025	0.2596	0.0124	0.0367	0.0008	256	107	234	10	233	5	99
19BJ06-2 Mylonitic granite														
1	0.10	0.0486	0.0010	0.3179	0.0074	0.0475	0.0011	127	49	280	6	299	7	106
2	0.50	0.0547	0.0027	0.3193	0.0161	0.0424	0.0010	398	108	281	12	268	6	95
3	0.14	0.0526	0.0011	0.3436	0.0080	0.0475	0.0011	310	48	300	6	299	7	100
4	0.15	0.0519	0.0012	0.3373	0.0085	0.0472	0.0011	279	53	295	6	297	7	101
5	0.07	0.0530	0.0011	0.3477	0.0081	0.0476	0.0011	331	48	303	6	300	7	99
6	0.64	0.0512	0.0025	0.3268	0.0164	0.0463	0.0011	248	110	287	13	292	6	102
7	0.27	0.0507	0.0024	0.3219	0.0153	0.0460	0.0011	228	105	283	12	290	6	102
8	0.11	0.0534	0.0012	0.3490	0.0085	0.0474	0.0011	344	50	304	6	299	7	98
9	0.35	0.0516	0.0013	0.3447	0.0094	0.0484	0.0011	268	57	301	7	305	7	101
10	0.24	0.0520	0.0014	0.3163	0.0092	0.0441	0.0010	286	62	279	7	278	6	100
11	0.21	0.0524	0.0016	0.3433	0.0107	0.0475	0.0011	304	67	300	8	299	7	100
12	0.70	0.0527	0.0035	0.3375	0.0226	0.0465	0.0011	315	144	295	17	293	7	99
13	0.13	0.0532	0.0012	0.3374	0.0084	0.0460	0.0010	339	51	295	6	290	6	98
14	0.22	0.0526	0.0014	0.3347	0.0093	0.0461	0.0010	313	59	293	7	291	6	99
15	0.11	0.0538	0.0017	0.3564	0.0115	0.0481	0.0011	362	69	310	9	303	7	98
16	0.39	0.0539	0.0014	0.3529	0.0096	0.0475	0.0011	367	57	307	7	299	6	97
17	0.31	0.0527	0.0015	0.3168	0.0094	0.0436	0.0010	316	63	279	7	275	6	98
18	0.21	0.0530	0.0013	0.3455	0.0090	0.0473	0.0010	328	55	301	7	298	6	99
19	0.09	0.0522	0.0013	0.3337	0.0089	0.0464	0.0010	294	56	292	7	292	6	100
20	0.18	0.0530	0.0014	0.3460	0.0097	0.0474	0.0010	328	59	302	7	298	6	99
21	0.58	0.0535	0.0048	0.3338	0.0298	0.0453	0.0011	349	190	292	23	286	7	98
22	0.28	0.0670	0.0021	0.4323	0.0142	0.0468	0.0011	837	65	365	10	295	6	76
23	0.58	0.0963	0.0023	0.5934	0.0148	0.0447	0.0010	1,553	43	473	9	282	6	32
24	0.38	0.0492	0.0014	0.3211	0.0096	0.0473	0.0010	159	66	283	7	298	6	105

10.1029/2022TC007689

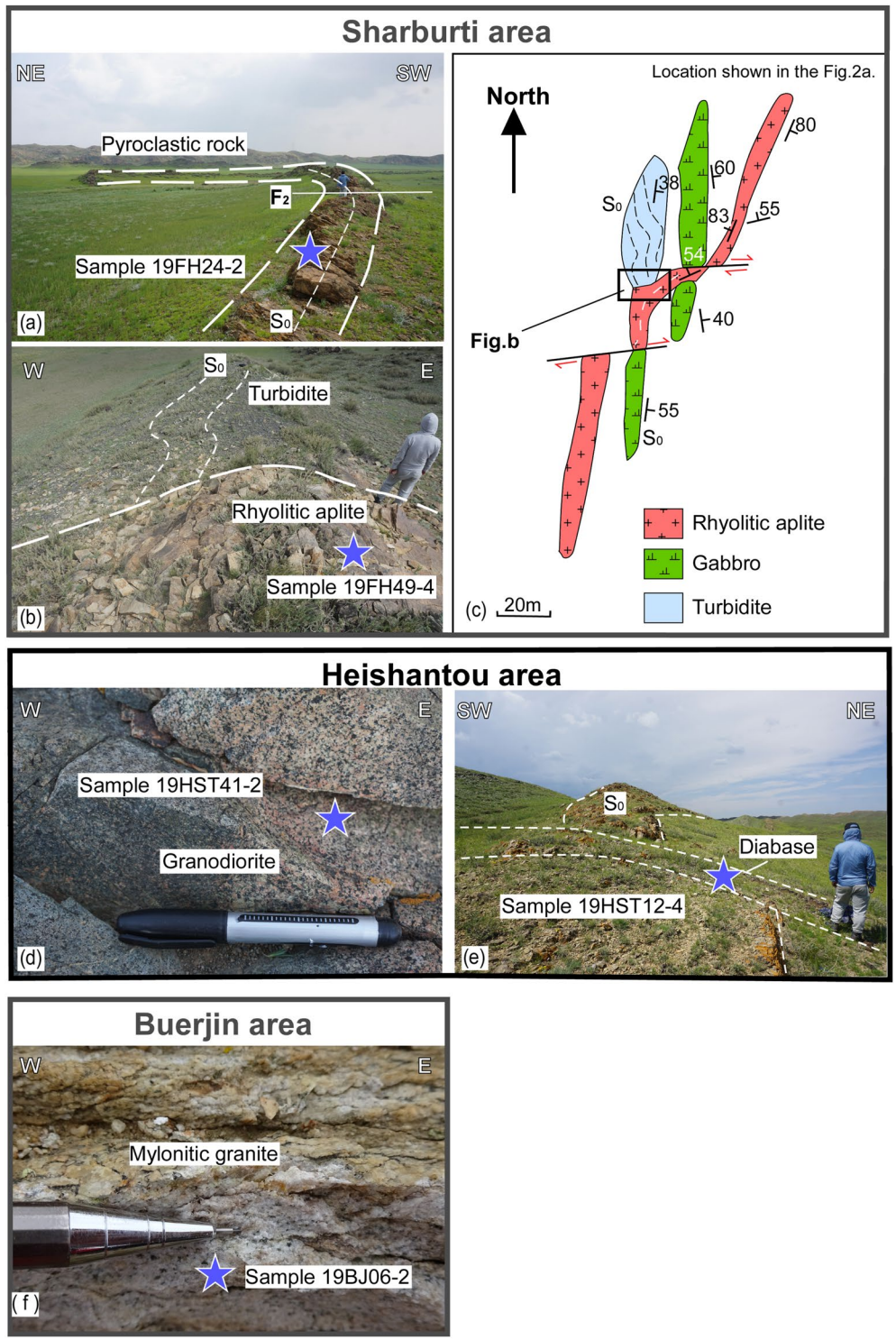

Figure 9. Representative field photographs of positions of samples used for U-Pb zircon dating. Sharburti area: (a) Structural position of folded pyroclastic bed (Sample 19FH24-2). (b) Position of rhyolitic aplite dyke (Sample 19FH49-4) cross-cutting folded bedding of host rock turbidite. (c) Interpretative structural sketch of dated rhyolite. Heishantou area: (d) and granodiorite sample 19HST41-2. (e) Field photograph of the diabase dyke (Sample 19HST12-4) cross-cutting the bedding. Buerjin area: (f) Photograph of mylonitic granite (Sample 19BJ06-2).

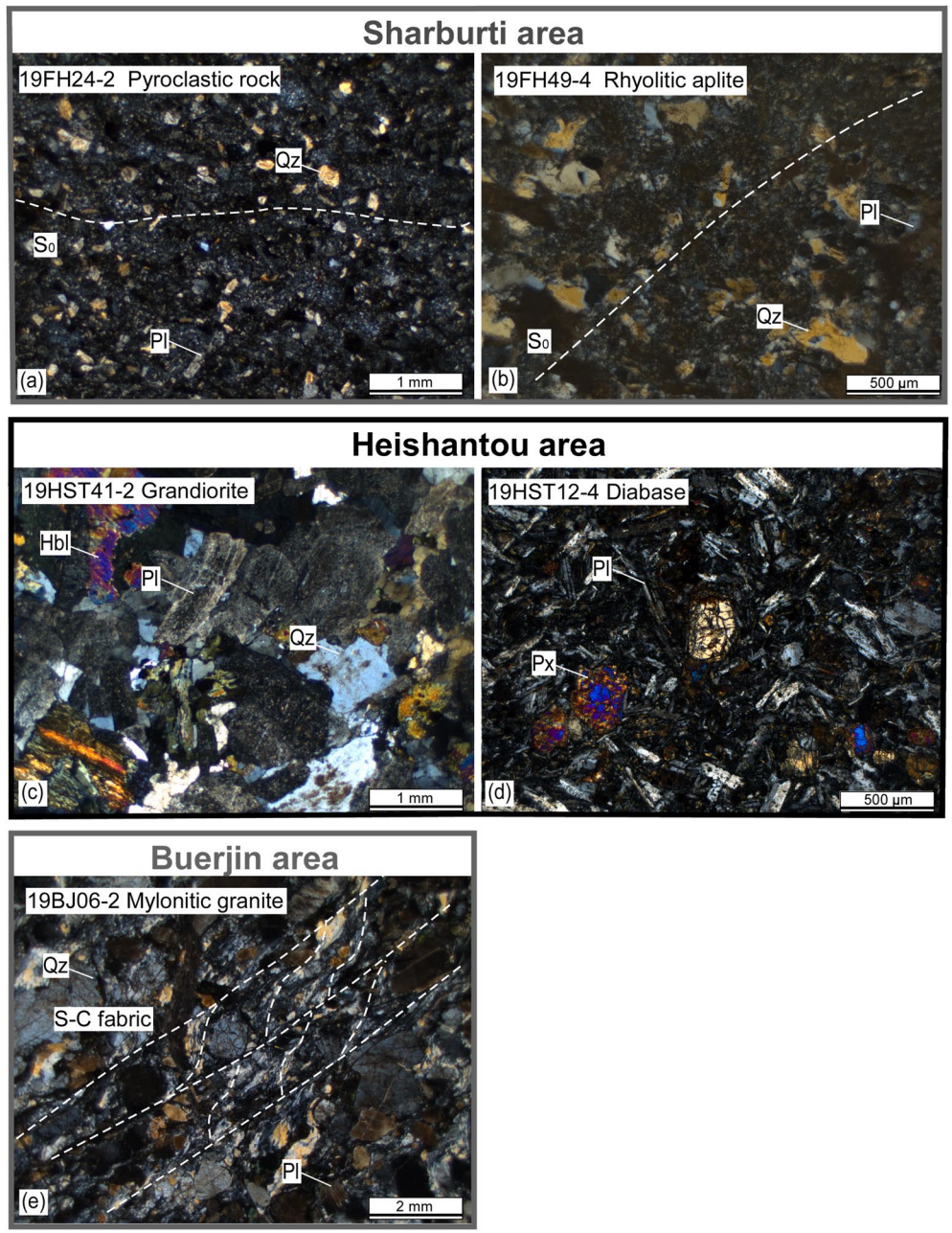

Figure 10. Micro-photographs of the selected samples for U-Pb zircon dating (crossed-nicols). (a and b) Pyroclastic and rhyolite dyke samples of the Sharburti area. (c and d) Granodiorite and diabase of the Heishantou area. (e) Mylonitized meta-granite of the Buerjin area. Q: Quartz; Pl: Plagioclase; Hb: Hornblende; Px: Pyroxene.

5.2. Heishantou Area: Pre-D2 Sample 19HST41-2, and Post-D2 Sample 19HST12-4

Sample 19HST41-2 was collected from a granodioritic intrusion in the central part of the Heishantou area (Figure 5a). In the field, the granodiorite intruded and truncated the axial plane of F1 folds affecting late Carboniferous volcano-sedimentary rocks but was slightly folded by the subsequent F2 chevron fold (Figure 5a). Therefore, the granodiorite is considered to have emplaced after D1 but before the D2 event. Both outcrop- and microscopic-scale observations show typical granitic texture without obvious signs of sub-solidus or post-solidus deformation (Figures 9d and 10c). Zircon grains show sub-euhedral crystal shapes and are 150–300 μm in length. CL images show oscillatory zoning texture and indicate a magmatic origin (Figure 11c). Th/U ratio varies from 0.48 to 0.80 (Table 1). Twenty-four analyses were conducted, and all the data yielded a $^{206}Pb/^{238}U$ weighted mean

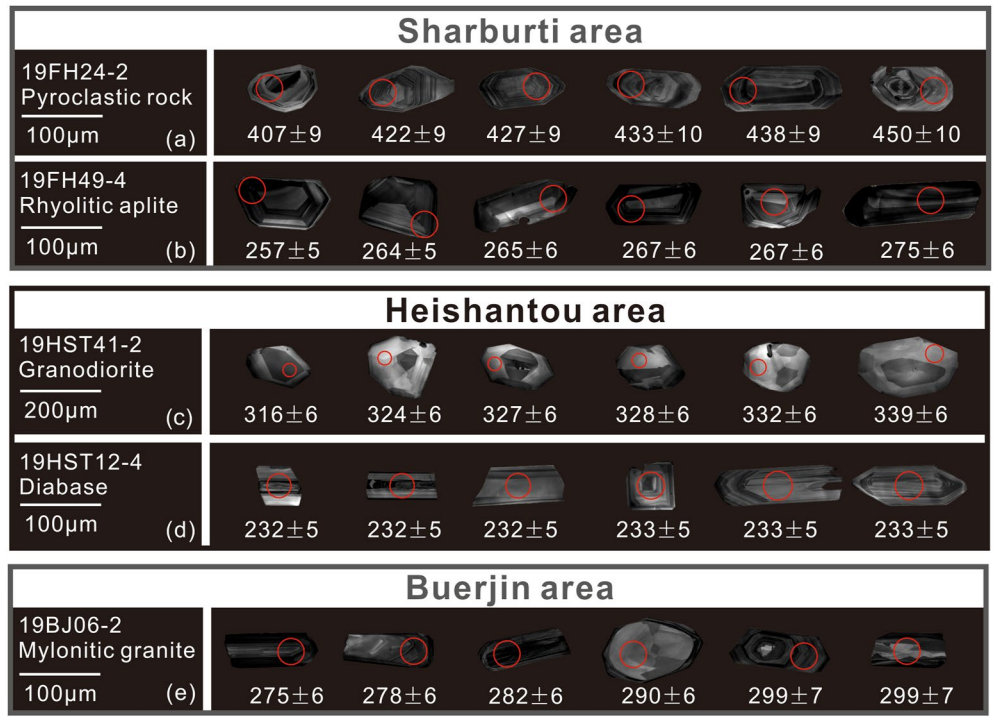

Figure 11. The CL images of zircons from studied samples.

age of 328 ± 4 Ma (MSWD = 1.02; Figure 12c). This age represents the crystallization age of the intrusion indicating that the pluton was emplaced between the regional D1 and D2 deformations.

Sample 19HST12-4 was collected from a mafic dyke that intruded into turbidites which were affected by F2 fold (Figure 5a). In the field, the mafic dyke crosscuts the bedding at a high angle (Figure 9e). Under the microscope, it shows a typical diabase texture characterized by the euhedral plagioclase with embedded subhedral pyroxene crystals (Figure 10d). Zircon grains extracted from the sample show euhedral and long prismatic crystals (60–180 μm with an aspect ratio up to 4:1) consistent with magmatic crystallization (Figure 11d). The Th/U ratios of the zircons are 0.10–1.09 and indicative of a magmatic origin (Table 1). On the Concordia diagram, 22 analyses yield a $^{206}Pb/^{238}U$ weighted mean age of 232 ± 2 Ma (MSWD = 0.034; Figure 12d), which is interpreted to represent the crystallization age of the diabase dyke. It also indicates that the regional D2 deformation ended before this time.

5.3. The Buerjin Area: Post-D1 and Pre-D2 Sample 19BJ06-2

As mentioned earlier, the Buerjin area is overprinted by a branch of the large-scale D2 Erqis fault zone (Figure 1b). Our field mapping has identified several mylonitic granitic intrusions, of which Sample 19BJ06-2 was collected from one mylonitic granite in the eastern Buerjin area (Figure 7a). In the field, it clearly intrudes and truncates the axial plane of the F1 fold but is affected by solid-state mylonitic fabric characterized by "S-C" features (Figures 10f and 11e). Zircon grains from the sample are euhedral to subhedral and have a length of 100–130 μm. CL images show oscillatory to sector zoning texture and indicate a magmatic origin (Figure 11e). Th/U ratio varies from 0.07 to 0.70 (Table 1). Total of 24 analyzed spots yielded $^{206}Pb/^{238}U$ ages ranging from 275 to 299 Ma (Table 1), with a weighted mean age of 292 ± 4 Ma (MSWD = 2.2, Figure 12e). It is interpreted as the crystallization age for the granitic intrusion post-dated D1 event and pre-dated D2 deformation.

6. Discussion

The Kazakhstan Orocline has been considered as the consequence of the mutual accretion of variable sizes of blocks, island arc fragments, and accretionary complexes (Abrajevitch et al., 2008; Xiao et al., 2018). Although

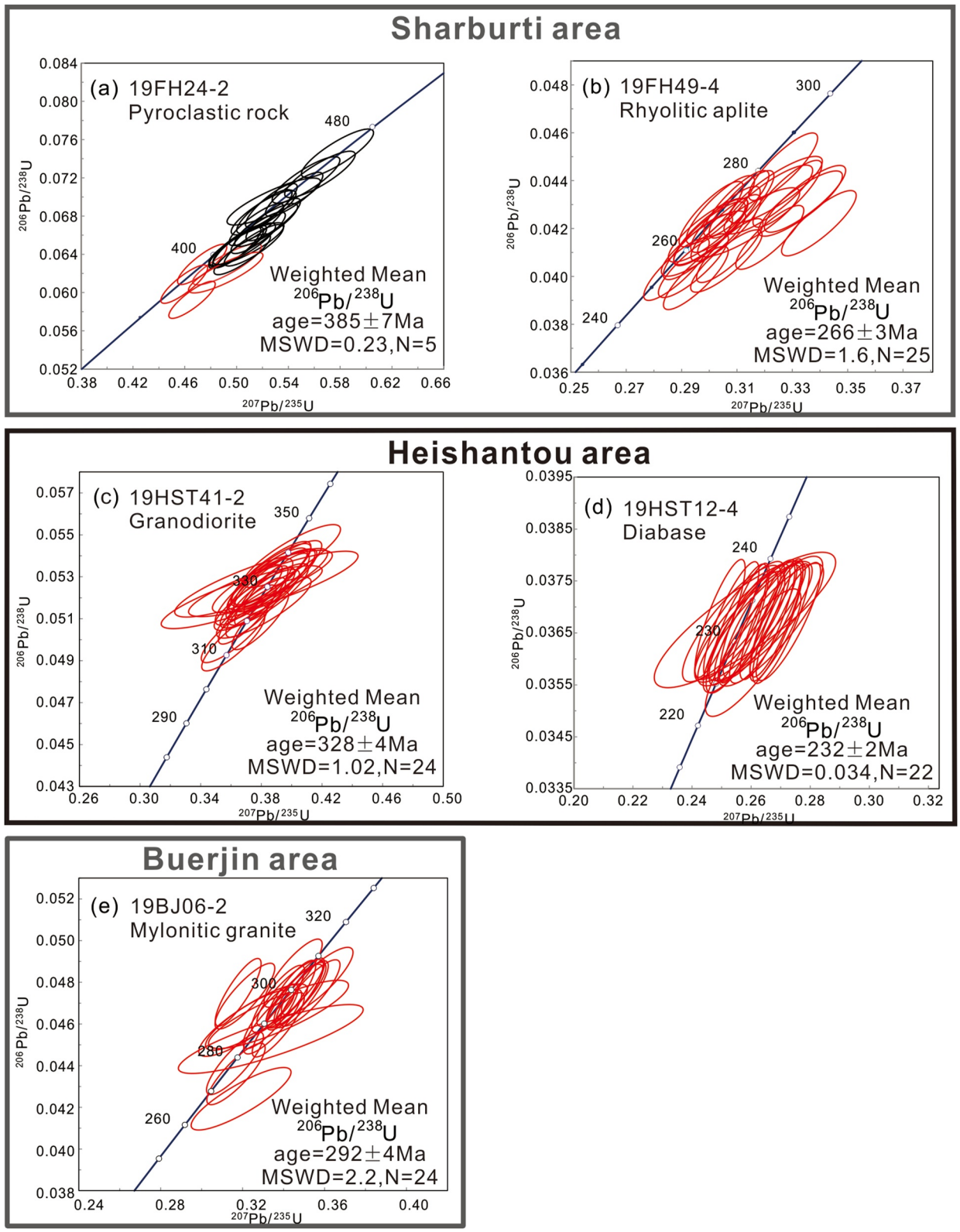

Figure 12. Concordia diagrams of LA-ICP-MS U-Pb zircon analytical results.

its formational mechanism was previously correlated to the forearc accretion and oroclinal bending of a single, long-lived subduction system (Şengör and Natal'in., 1996; Şengör et al., 1993; Şengör et al., 2018), more and more scholars have reached an agreement that the orocline was formed through subduction and accretion of several oceanic basins, microcontinents and island arcs along multiple subduction zones (Windley et al., 2007; Xiao et al., 2010, 2018). It was also proposed that multiple cycles of roll-back of the subducted slabs played a key role in forming the Kazakhstan Orocline (Xiao et al., 2018). Most recently, a disharmonic structural pattern related to the northern limb of the Kazakstan Orocline was termed a second-order curvature and named the West Junggar Orocline by P. Li et al. (2018).

Based on available geological and paleomagnetic data of the Kazakhstan Orocline, P. Li et al. (2017, 2018) proposed that the West Junggar Orocline was formed through two stages of bending events from Devonian to Permian. According to these authors, during the late Devonian to early Carboniferous bending stage, the Junggar ocean subduction zone was subjected to slab roll-back. This is indicated by the retreating of the Balkhash-Yili Arc to the east with respect to the westerly Devonian Volcanic Belt. This stage was associated with the pinning of the subduction system along the southern limb of the Kazakhstan Orocline and the synchronous rapid and asymmetric slab roll-back along the northern limb (P. Li et al., 2017, 2018). The second stage of bending occurred in the late Carboniferous to Permian, during which the Junggar Block was considered as another pin that affected the successively southward roll-back of the northern limb, to ultimately produce the West Junggar Orocline (P. Li et al., 2017, 2018).

However, such an interpretation is not fully supported by our new field mapping results, structural and geophysical data. In this study, our field mapping in the Sharburti, Heishantou, and Buerjin areas has revealed that they are characterized by different lithological units of different ages, indicating that they may have experienced independent histories prior to their mutual amalgamation. In addition, early to late Carboniferous orogenic fabrics described in this work as well as those reported from the West Karamay, Toli Units and Boshchekul-Chingiz Arc (Choulet et al., 2012b; Song et al., 2020; P. Zhang et al., 2018b) show important differences between early Paleozoic units to the south and late Paleozoic units to the north that can hardly be explained by a roll-back driven oroclinal bending. There are also considerable differences in the later Permian deformation in the south where it was related to E-W folding and sinistral NE-SW strike-slip faulting and in the north where E-W folding and E-W sinistral shearing are reported. Altogether, Carboniferous and Permian deformations revealed significant variations from south to north and complex geometrical and kinematical patterns that are not fully compatible with the above proposed roll-back scenario.

In order to contribute to the discussion related to the origin of the disharmonic structure of the West Junggar Orocline we discuss first the possible timing of various structures across the studied profile, the geometry of principal geophysical anomalies and lineaments together, and the kinematic interpretation of orogenic fabrics across the whole West Junggar. All these datasets are used to propose a model of amalgamation of individual arc chains and accretionary wedges followed by their polyphase deformation related to the progressive northward movement of the Junggar Block.

6.1. Timing Constraints on the Regional D1 and D2 Deformations

To constrain the regional deformational history, we have summarized all the published ages of the three areas (Table 2). Combining the previous ages with our new age data, we suggest that the three areas may have experienced independent evolutionary histories before they mutually accreted with one another by late Carboniferous.

In the Sharburti area (Boshchekul-Chingiz Arc), the northern Ordovician-Devonian unit experienced both D1 and D2 deformations (Figure 13a). Our new dating results on the pyroclastic rocks of this unit gave a zircon age of 385 ± 7 Ma (Figure 2a), indicating that the regional D1 deformation should occur after ~385 Ma. In this area, previous geochronological data also reveals the zircon age of 375 ± 5 Ma for the youngest Devonian turbidite (Song et al., 2020), which can be used to further constrain the maximum age of the D1 deformation. Based on our mapping result, the southern Permian unit only records the regional D2 deformation (Figure 4). Therefore, the available oldest zircon age of 298 ± 3 Ma obtained from the Permian volcanic rocks leads us to constrain the minimum age of D1 and maximum age of D2 deformations (G. Liu et al., 2018). Moreover, the minimum age of the D2 deformation can be constrained by the 266 ± 3 Ma undeformed N-S rhyolitic aplite dykes that truncated the regional D1 fabrics but can be associated with late stages of F2 folding (Figure 9c). Therefore, the

Table 2
Zircon U–Pb Ages in the Three Representative Areas

Sample	Lithology	Age	Method	Data source
Sharburti area				
HG-3	Gabbro	472 ± 8 Ma	SHRIMP	Zhang et al. (2010)
19FH24-2	Pyroclast rock	385 ± 7 Ma	LA-ICP-MS	This study
DJ325	Greywacke	388 ± 10 Ma	LA-ICP-MS	Choulet et al. (2012a, 2012b, 2012c)
16-EM-147	Turbidite	375 ± 5 Ma	LA-ICP-MS	Song et al. (2020)
PKTW02	Rhyolite	298 ± 3 Ma	LA-ICP-MS	Liu et al. (2018)
19FH49-4	Rhyolite	266 ± 3 Ma	LA-ICP-MS	This study
Heishantou area				
	Rhyolite	338 ± 1 Ma	LA-ICP-MS	Li et al. (2020)
19HST41-2	Granodiorite	328 ± 3 Ma	LA-ICP-MS	This study
Kaerjiao pluton	Granite	303 ± 8 Ma	SHRIMP	Zhou et al. (2008)
19HST12-4	Diabase	232 ± 2 Ma	LA-ICP-MS	This study
Buerjin area				
L14FY89	Slate	399 Ma	LA-ICP-MS	Li et al. (2017)
K3815-3	Gabbro	364 ± 5 Ma	LA-ICP-MS	Wang et al. (2012)
K3815-7-3	Gneissic granite	355 ± 7 Ma	LA-ICP-MS	Wang et al. (2012)
09Al25	Gabbro	332 ± 2 Ma	LA-ICP-MS	Zhang et al. (2012)
L14FY91	Meta-graywacke	324 Ma	LA-ICP-MS	Li et al. (2017)
08TW03	Granite	300 ± 2 Ma	LA-ICP-MS	Zhang et al. (2012)
19BJ06-2	Mylonitic granite	292 ± 4 Ma	LA-ICP-MS	This study
08 TW 02	Granodiorite	286 ± 2 Ma	LA-ICP-MS	Zhang et al. (2012)
Buerjin3198	Monzogranite	268 ± 5 Ma	LA-ICP-MS	Tong et al. (2014)

D1 deformation most likely developed in the interval between late Devonian to late Carboniferous (375-298 Ma), while the D2 deformation occurred during the early Permian (298-266 Ma) (Figures 13b and Table 2). These time intervals corroborate the results of Song et al. (2020) who proposed a deformation of the subduction wedge dipping beneath the Boshchekul-Chingiz Arc to the south at Carboniferous time. This event was followed by Permian-Triassic deformation related to an accretion of subduction wedge beneath the northern Carboniferous Zharma-Saur Arc.

In the Heishantou area (Zharma-Saur Arc), the Devonian-Carboniferous sequences experienced two stages of folding (Figure 5a). The maximum age of the D1 deformation can be constrained by zircon age of 338 ± 1 Ma from the intraformational rhyolite sill (H. Li et al., 2020; Figures 5a and 5b). S0 bedding steepened by F1 folds is crosscut by granodiorite intrusion, which implies that the latter is younger than D1. The minimum age of D1 and maximum age of the subsequent D2 deformation is therefore constrained by the granodioritic intrusion of 328 ± 4 Ma (Figure 5a). However, the minimum age of the D2 deformation of this area can only be constrained by the undeformed 232 ± 2 Ma mafic dyke that intruded the limb of the F2 synformal fold (Figure 5a). Therefore, in the Heishantou area the regional D1 deformation most probably developed in Carboniferous (338-328 Ma), whereas the D2 deformation developed between the late Carboniferous and Triassic (328-232 Ma) (Figure 13b and Table 2).

In the Buerjin area, the northern Erqis-Zaysan zone and the southern Zharma-Saur Arc were experienced both F1 folding and D2 Erqis fault zone deformations (Figure 7a). Previous dating results on the deformed meta-graywacke rock gave the zircon U-Pb age of 324 Ma (P. Li et al., 2017), indicating that the regional D1 deformation should occur sometime after 324 Ma (Table 2). The maximum age of the subsequent D2 deformation is further constrained by the mylonized granite that gave a zircon U-Pb age of 292 ± 4 Ma (Figures 7a and 10f). The end of D2 deformation is possibly constrained by undeformed 268 ± 5 Ma post-tectonic granitic intrusions

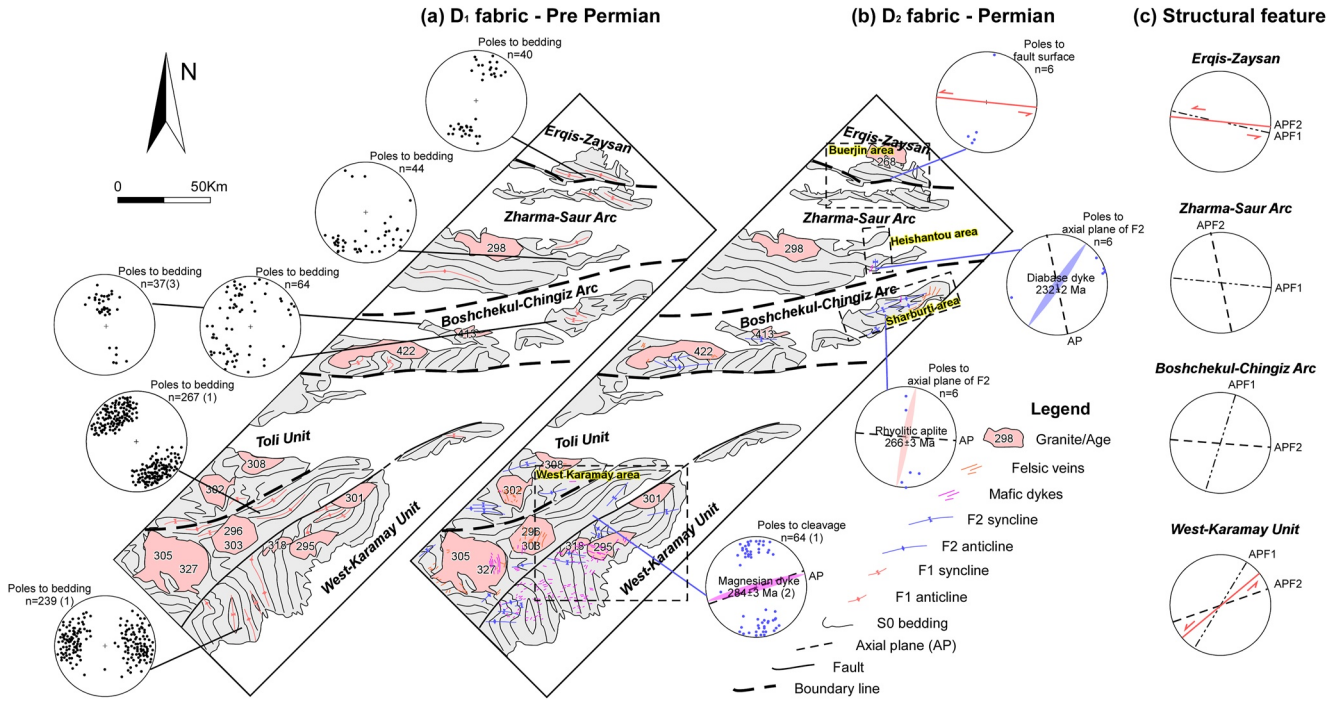

Figure 13. (a) The regional distribution of S0 bedding and of the D1 structures in the West Junggar. (b) D2 structural patterns and orientation of geochronologically constrained dykes. (c) Restoration of D1 fold axial planes of fabrics and D2 fold axial planes and late faults across the West Junggar. Data from: (1) Zhang et al., 2018; (2) Yin et al., 2013; (3) Song et al., 2020.

(Tong et al., 2014; Figure 7a and Table 2). Generally in the Buerjin area, the D1 deformation most likely occurred during the late Carboniferous (324-292 Ma), while the D2 deformation developed during the early Permian (292-268 Ma) (Figure 13b and Table 2).

In summary, we utilized synthetic approaches of structural geology and geochronology to constrain the timing and kinematics of the regional D1 and D2 deformation in the northern part of the West Junggar (Figure 13). These data corroborate the findings of Choulet et al. (2012b) and P. Zhang et al. (2018b) who proposed that the first shortening of the Devonian and Carboniferous wedge of the West Karamay Unit occurred during the early to late Carboniferous time. Permian folding and sinistral faulting followed this early deformation phase. Overall, the regional D1 deformation was most likely Carboniferous, and the D2 deformation was Permian in age. Timing of D1 is further evidenced by the coeval arc-related magmatism that was correlated to the late stage of the Junggar Ocean subduction, whereas the ending time of D2 was limited by emplacement ages of extensive Permian post-collisional A-type granites (Zheng et al., 2019, 2020).

6.2. Tectonic Interpretation of Geophysical Data

Careful analysis of gravity and magnetic anomalies better constrains the spatial extent of arc chains, accretionary wedges and basement blocks covered by sediments and strike and dip of main tectonic boundaries (Guy et al., 2020, 2021). The location of the Erqis-Zaysan Zone, Boshchekul-Chingiz and Zharma-Saur fore-arcs and the West Karamay accretionary wedges mostly coincide with areas of intermediate to low magnetic and gravity signals. The magnetic highs correlate with the Zharma-Saur Arc and to a lesser extent with the Boshchekul-Chingiz Arc and Toli Unit. The Zharma-Saur Arc is delineated by important deep-seated gravity anomalies. Important gravity high straddle the boundary between the West Karamy Unit and the Junggar Block, which may locate the limit of the Junggar Block underneath westerly West Junggar (Figure 14a). A prominent crustal-scale contrast can be established along the boundary between the Junggar Block and the West Junggar, which can be interpreted as an important subvertical to slightly NW dipping tectonic boundary. In contrast, the Hongguleleng, Xiemisitai, Barleike and Mayile faults in the West Junggar do not display such significant geophysical contrasts and indicate that they are shallow thrust faults. The inner part of the Junggar Block comparatively exhibits low amplitude and low frequency magnetic and gravity signals compared to the West Junggar.

10.1029/2022TC007689

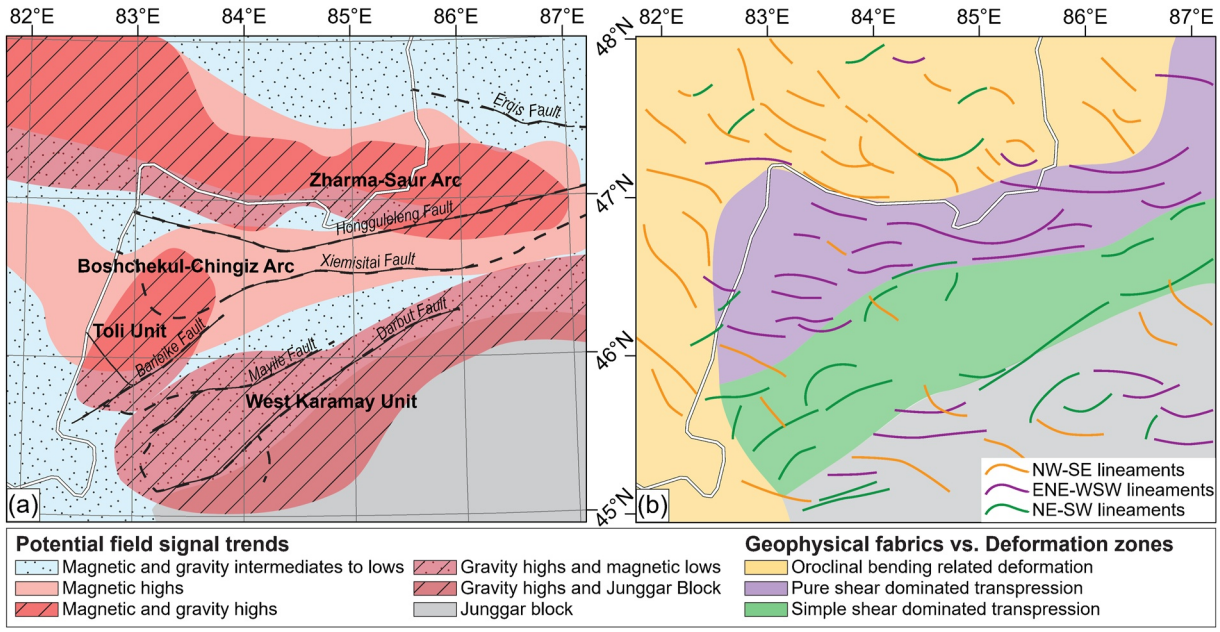

Figure 14. Correlation of potential field trends with the tectonic and deformation zones. (a) Distribution of the patterns of magnetic and gravity highs and lows related to shapes of arc chains, Junggar basement and accretionary wedges. (b) Subdivision of magnetic and gravity lineaments into three groups in order to visualize orocline related compressive fabrics and simple and pure shear transpression fabrics related to indentation. Dominant type of orogenic fabrics are shown in the background.

The magnetic and gravity lineaments generally reflect the intensity and orientation of deformation overprints (Guy et al., 2021). In the East Junggar and the Chinese Altai, these authors identified two types of geophysical lineaments correlated to early Carboniferous and Permian tectonic events, respectively. Using the similar approach, three specific groups of lineaments in the West Junggar were defined (Figure 14b). Group 1 of NW-SE-oriented geophysical fabrics occurs in the west and north of the studied area and spatially coincide with the Kazakhstan area, the northern part of the Zharma-Saur Arc and the western part of the Erqis-Zaysan Zone, typical for the Kazakhstan Orocline bending related deformation zone, which is subparallel to its northern limb. These fabrics are interpreted to reflect the primary accretionary fabrics related to mutual amalgamation of arc chains. Group 2 of NE–SW-oriented lineaments form a wide zone along the western margin of the Junggar Block, spatially coinciding with the West Karamay, Mayile-Tangbale Units and the eastern part of the Toli Unit, all of which are grouped into the eastern branch of the West Junggar Orocline. The Group 2 lineaments are interpreted to result from sinistral transpression in the sense of Choulet et al. (2012b) and P. Zhang et al. (2018b). Group 3 lineaments are represented by ENE–WSW-oriented geophysical fabrics in the central part of the region represented by eastern terminations of Boshchekul-Chingiz and Zharma-Saur Arc chains and its orientation coincides with the trend of axial planes of F2 folds affecting the Boshchekul-Chingiz Arc (Figure 14b).

6.3. Orogenic Structures and Rigid Block Indentation

Our study shows that the D1 fabrics in the whole transect are related to horizontal compression, although they display considerable differences in finite orientation (Choulet et al., 2012b; P. Zhang et al., 2018b, this work). After restoring their pre-D2 orientation, the F1 folds in the West Karamay Unit and the Boshchekul-Chingiz Arc were oriented along NE-SW to N-S (Figure 13a), which is largely sub-parallel to the eastern limb of West Junggar Orocline (Figure 1a). On the other hand, the F1 folds in the Zharma-Saur Arc (Heishantou area) and the Erqis-Zayan Zone (Buerjin area) are trending along E-W (Figure 13a).

Similarly, the D2 structures show important differences (Figure 13b). In the West Karamay Unit and Boshchekul-Chingiz Arc, the F2 folds show E-W trending axial planes and/or axial planar cleavage that indicate an N-S compression. In the West Karamay area, this folding was connected to the activity of the Permian sinistral NE-SW Darbut fault (Choulet et al., 2012b). However, in the Zharma-Saur Arc the late D2 deformation is related to large-scale chevron folding under the ENE-WSW compression, while further north in the D2 is characterized by an E-W sinistral faulting (Figures 13b and 13c).

These differences can be explained in two stages of evolution related to: (a) accretion-amalgamation history of individual units forming northern limb of the Kazakstan Orocline (Figures 13a and 15a); (b) indentation of amalgamated units by the rigid Junggar indenter related to overall N-S convergence in the current coordinates (Figures 13b and 15b). During the Carboniferous accretion, the Zharma-Saur Arc and Erqis-Zaysan accretionary complex were shortened in NEN-SWS direction and this orientation was not modified by later deformation events. Carboniferous deformation brought these units in ENE-WSW orientation, which is also represented by Group 1 geophysical lineaments. However, the pre-D2 ENE-WSW orientation of early Carboniferous F1 upright folds in the West-Karamay Unit, Toli Unit and Boshchekul-Chingiz Arc can be best explained by their rotation into parallelism with eastern NE-SW striking boundary of the Junggar Block. In this way, the pre-indentation orientation of the D1 fabrics was also ENE-WSW similar to the younger Zharma-Saur Arc and the Erqis-Zaysan complex to the north. This indicates that prior to the indentation event, all units forming the northern limb of the Kazakhstan Orocline suffered severe D1 NEN-SWS shortening (Figures 13a and 15a). Consequently, the horizontal stress generating folds and cleavage has to be transmitted across the whole West Junggar complex during the late Carboniferous, which is not entirely compatible with the roll-back hypothesis. The later subduction mode is more compatible with extensional tectonics and not compression, which is characteristic for advancing subduction mode or directly to collision (e.g., Collins, 2002).

The D2 deformation is compatible with deformation of crust in front of progressively moving indenter (Figures 13b and 13c, and 15b). The formation of E-W trending folds and simultaneous activity of a series of NE-SW trending sinistral strike-slip faults (e.g., Darbut Fault, Mayile Fault and Barleike Fault; Figure 1b; Choulet et al., 2012b) are compatible with partitioned transpressive deformation parallel to the NE-SW trending boundary of the Junggar indenter (Figures 13b and 15b). The formation of E-W trending F2 folds (Sharburti area) together with the orientation of Group 3 geophysical lineaments can be regarded as an expression of a pure shear dominated transpression for 40°–50° convergence angle (Ježek et al., 2002; Lexa et al., 2004). This configuration is typical for pure shear shortening in front or a region far from the indenter, while the simple shear component close to the indenter boundary is accommodated by partitioned faulting and drag folding (Figure 15b).

The ca. 290-260 Ma age of the D2 shortening is best expressed by the dating of rhyolitic dykes perpendicular to the axial planes of F2 folds in the Sharburti area. It is also compatible with the dating and orientation of granite porphyry and pegmatitic dykes intruding the Chinese Altai (Jiang et al., 2019; Shu et al., 2022). These observations indicate that the early Permian deformation of the Chinese Altai units to the north likely operated in the same coordinates and direction as that D1 in the south. Consequently, we can regard the D1 deformation as the result of initial Carboniferous shortening and the D2 as a perturbation of the deformation field in front (pure shear component) or along (partitioned simple shear components) a rigid Junggar indenter.

Followed the early Permian compression, the mutual displacement of the Tuva-Mongol and Kazakhstan Oroclines probably triggered the large-scale sinistral Erqis fault that reworked the D1-D2 fabrics in the Burjin area (Figures 15b and 15e).

6.4. Oroclinal Bending and Junggar Block Indentation Model

The data presented in this study are compatible with the subduction of the Junggar relict ocean basin beneath the southern Boshchekul-Chingiz Arc, which is evidenced by the existence of Permian arc-related igneous rocks of the region (Gao et al., 2014). Our and previously published data (Choulet et al., 2012b; P. Zhang et al., 2018b) indicate that the arc chains and accretionary wedges were amalgamated and deformed by upright folds during the late Carboniferous. Continuous northward subduction of the Junggar relict ocean basin led the rigid Junggar Block to finally collide with previously amalgamated arc chains (Figure 15b).

The structural and geophysical data show the existence of three domains with contrasting structural evolution and orientations of geophysical lineaments (Figures 13 and 14) compatible with domains originating from oroclinal bending, sinistral partitioned transpression and pure shear dominated transpression. We propose that this finite strain pattern was formed during two stages. During the first stage, WNW-ESE oriented arc chains and accretionary wedges of the southern part of the West Junggar complex rotated into parallelism with NE-SW trending western margin of the Junggar indenter (Figure 15c). The "U" shaped form of West Junggar Orocline originated due to active oroclinal bending of layers without the change of thickness of individual units (Figure 15d). The active oroclinal bending pattern was primarily controlled by the horizontal indentation perpendicular to the subduction/accretionary fabric, for example, by the entry of the Junggar Block into a subduction zone. When the

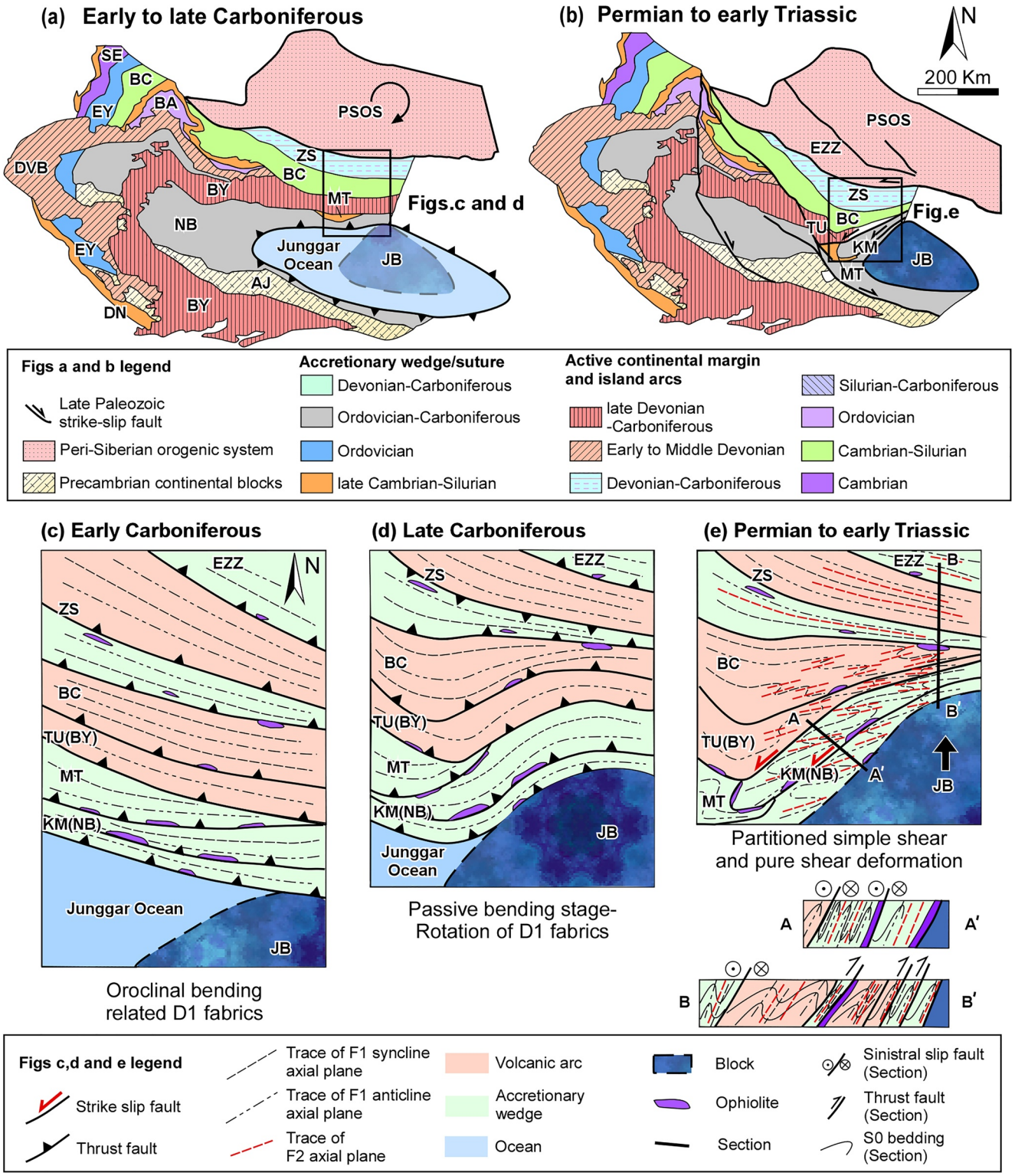

Figure 15. (a) Amalgamation of arc chains and accretionary complexes shaping the Kazakhstan Orocline until the late Carboniferous. (b) Northward indentation of the Junggar Block in Permian leading to anticlockwise rotation of the Kazakhstan Orocline limb producing "U" shaped West Junggar Orocline. (c) Schematic map of accreted arcs and accretionary wedges affected by Early Carboniferous F1 folds in the West Junggar. (d) Schematic map showing anticlockwise rotation of the northern limb of the Kazakhstan Orocline–active oroclinal bending stage. (e) Partitioning of deformation into simple shear dominated transpression (sinistral faulting and drag folding) and pure shear dominated transpression (upright folding) during late stages of indenter progression. PSOS: Peri-Siberian orogenic system; DN: Dzhalair-Naiman; SE: Selety Arc; EY: Erementau-Yili belt; BA: Baydaulet-Akbstau Arc; DVB: Early to middle Devonian volcanic belt; BY: Balkhash-Yili Arc; AJ: Aktau-Junggar; NB: N. Balkhash; EZZ: Erqis-Zaysan Zone; ZS: Zharma-Saur Arc; BC: Boshchekul-Chingiz Arc; TU: Toli Unit; MT: Mayile-Tangbale Unit; KM: West Karamay Unit; JB: Junggar Block.

indenter progressed further to the north, the deformation partitioned into zone of sinistral simple shear dominated transpression parallel to the indenter boundary as the cross-section A and pure shear dominated transpression far from the indenter or close to its apical part as the cross-section B (Figure 15e). Only there, the deformation resulted in massive shortening of arc chains layers (Figure 15e).

7. Conclusions

Based on structural, geochronological and revised geophysical data in the northern West Junggar, we can reach the following conclusions.

- Different arc chains experienced independent evolutional histories before they accreted with one another and generated the regional D1 deformation in the late Carboniferous. Subsequent D2 shortening event occurred in Permian and produced variable superimposed structures, including a crescent-mushroom-like fold in the Boshchekul-Chingiz Arc and superposed folding and sinistral strikes slip faulting in West Karamay Unit. Chevron fold in the Zharma-Saur Arc, and crustal-scale Erqis-Zaysan sinistral strike-slip shear zone in the Buerjin area possibly originated due to a modified stress regime related to juxtaposition of Kazakhstan and Tuva-Mongol Oroclines during the late Permian and Triassic.
- Although the roll-back process was potentially responsible for forming the basic framework of the Kazakhstan Orocline until Carboniferous, the northward shortening associated with the indentation of the Junggar Block into the arc chains played an important role in producing the disharmonic structural pattern of the West Junggar in Permian.
- Indentation of the rigid blocks or plates may represent a type of important geodynamic mechanism accompanying the Permian collisional process forming finite strain pattern of the CAOB.

Data Availability Statement

The zircon U-Pb data used for constraint the timing of the regional D1 and D2 deformations in the study are available at Supporting Information_Tables. The gravity and magnetic data used in this study come respectively from the EGM08 (available at http://earth-info.nga.mil/GandG/wgs84/gravitymod/egm2008/) and EMAG2 (available at https://www.ngdc.noaa.gov/geomag/emag2.html) models.

Acknowledgments
This study was financially supported by the National Natural Science Foundation of China (42025204); Grant Agency of the Czech Republic (GAČR EXPRO grant GX19-27682X); Guangdong Province Introduced Innovative R&D Team of Geological Processes and Natural Disasters around the South China Sea (2016ZT06N331), International Partnership Program of Chinese Academy of Sciences (132744KYSB20190039), and the Third Xinjiang Scientific Expedition Program (2022xjkk1301). The gravity and magnetic data used in this study come respectively from the EGM08 (available at http://earth-info.nga.mil/GandG/wgs84/gravitymod/egm2008/) and EMAG2 (available at https://www.ngdc.noaa.gov/geomag/emag2.html) models.

References

Abrajevitch, A., Van der Voo, R., Bazhenov, M. L., Levashova, N. M., & McCausland, P. J. (2008). The role of the Kazakhstan Orocline in the late Paleozoic amalgamation of Eurasia. *Tectonophysics*, *455*(1–4), 61–76. https://doi.org/10.1016/j.tecto.2008.05.006

Archibald, N., Gow, P., & Boschetti, F. (1999). Multiscale edge analysis of potential field data. *Exploration Geophysics*, *30*(1–2), 38–44. https://doi.org/10.1071/EG999038

Broussolle, A., Sun, M., Schulmann, K., Guy, A., Aguilar, C., Štípská, P., et al. (2019). Are the Chinese Altai "terranes" the result of juxtaposition of different crustal levels during Late Devonian and Permian orogenesis? *Gondwana Research*, *66*, 183–206. https://doi.org/10.1016/j.gr.2018.11.003

Bureau of Geology and Mineral Resources of Xinjiang Uygur Autonomous Region (1993). Regional geology of Xinjiang Uygur Autonomous Region. (in Chinese). In *People's Republic of China, ministry of geology and mineral resources, Geological Memoirs, Series* (Vol. 1, p. 206). Geological Publishing House.

Buslov, M. M., Fujiwara, Y., Iwata, K., & Semakov, N. N. (2004). Late Paleozoic-early Mesozoic geodynamics of Central Asia. *Gondwana Research*, *7*(3), 791–808. https://doi.org/10.1016/S1342-937X(05)71064-9

Chen, Y. C., Xiao, W. J., Windley, B. F., Zhang, J. E., Sang, M., Li, R., et al. (2017). Late Devonian-early Permian subduction-accretion of the Zharma-Saur oceanic arc, West Junggar (NW China): Insights from field geology, geochemistry and geochronology. *Journal of Asian Earth Sciences*, *145*, 424–445. https://doi.org/10.1016/j.jseaes.2017.06.010

Choulet, F., Cluzel, D., Faure, M., Lin, W., Wang, B., Chen, Y., et al. (2012a). New constraints on the pre-Permian continental crust growth of Central Asia (West Junggar, China) by U-Pb and Hf isotopic data from detrital zircon. *Terra Nova*, *24*(3), 189–198. https://doi.org/10.1111/j.1365-3121.2011.01052.x

Choulet, F., Faure, M., Cluzel, D., Chen, Y., Lin, W., & Wang, B. (2012b). From oblique accretion to transpression in the evolution of the Altaid collage: New insights from West Junggar, northwestern China. *Gondwana Research*, *21*(2-3), 530–547. https://doi.org/10.1016/j.gr.2011.07.015

Choulet, F., Faure, M., Cluzel, D., Chen, Y., Lin, W., Wang, B., & Jahn, B. M. (2012c). Architecture and evolution of accretionary orogens in the Altaids collage: The early Paleozoic West Junggar (NW China). *American Journal of Science*, *312*(10), 1098–1145. https://doi.org/10.2475/10.2012.02

Choulet, F., Faure, M., Cluzel, D., Chen, Y., Lin, W., Wang, B., & Xu, B. (2016). Toward a unified model of Altaids geodynamics: Insight from the Palaeozoic polycyclic evolution of west junggar (nw China). *Science China Earth Sciences*, *59*(1), 25–57. https://doi.org/10.1007/s11430-015-5158-7

Collins, W. J. (2002). Nature of extensional accretionary orogens. *Tectonics*, *21*(4), 6-1–6-12. https://doi.org/10.1029/2000tc001272

Feng, Y., Coleman, R. G., Tilton, G., & Xiao, X. (1989). Tectonic evolution of the West Junggar Region Xinjiang China. *Tectonics*, *8*(4), 729–752. https://doi.org/10.1029/tc008i004p00729

Gao, R., Xiao, L., Franco, P., Wang, G., He, X., Yang, G., & Yan, S. (2014). Carboniferous–Permian extensive magmatism in the West Junggar, Xinjiang, northwestern China: Its geochemistry, geochronology, and petrogenesis. *Lithos*, *204*, 125–143. https://doi.org/10.1016/j.lithos.2014.05.028

Guy, A., Schulmann, K., Soejono, I., Holzrichter, N., Lexa, O., & Munschy, M. (2021). Structures and geodynamics of the Mongolian tract of the Central Asian Orogenic Belt constrained by potential field analyses. *Gondwana Research*, *92*, 26–53. https://doi.org/10.1016/j.gr.2020.11.016

Guy, A., Schulmann, K., Soejono, I., & Xiao, W. (2020). Revision of the Chinese Altai-East Junggar terrane accretion model based on geophysical and geological constraints. *Tectonics*, *39*(4). https://doi.org/10.1029/2019tc006026

Holden, D. J., Archibald, N. J., Boschetti, F., & Jessell, M. W. (2000). Inferring geological structures using wavelet-based multiscale edge analysis and forward models. *Exploration Geophysics*, *31*(4), 617–621. https://doi.org/10.1071/EG00617

Hornby, P., Boschetti, F., & Horowitz, F. G. (1999). Analysis of potential field data in the wavelet domain. *Geophysical Journal International*, *137*(1), 175–196. https://doi.org/10.1046/j.1365-246x.1999.00788.x

Hu, W., Li, P., Sun, M., Safonova, I., Jiang, Y., Yuan, C., & Kotler, P. (2021). Provenance of late Paleozoic sedimentary rocks in eastern Kazakhstan: Implications for the collision of the Siberian margin with the Kazakhstan collage. *Journal of Asian Earth Sciences*, *232*, 104978. https://doi.org/10.1016/j.jseaes.2021.104978

Jahn, B.-M. (2004). The Central Asian Orogenic Belt and growth of the continental crust in the Phanerozoic. *Geological Society, London, Special Publications*, *226*(1), 73–100. https://doi.org/10.1144/gsl.Sp.2004.226.01.05

Ježek, J., Schulmann, K., & Thompson, a. B. (2002). *Strain partitioning in front of an obliquely convergent indenter* (Vol. 1). EGU Stephan Mueller Special Publication Series.

Jiang, Y. D., Schulmann, K., Sun, M., Weinberg, R. F., Štípská, P., Li, P. F., et al. (2019). Structural and geochronological constraints on Devonian suprasubduction tectonic switching and Permian collisional dynamics in the Chinese Altai, Central Asia. *Tectonics*, *38*(1), 253–280. https://doi.org/10.1029/2018tc005231

Khromykh, S. V., Semenova, D. V., Kotler, P. D., Gurova, A. V., Mikheev, E. I., & Perfilova, A. A. (2020). Orogenic volcanism in eastern Kazakhstan: Composition, age, and geodynamic position. *Geotectonics*, *54*(4), 510–528. https://doi.org/10.1134/s0016852120040044

Kröner, A., Kovach, V., Belousova, E., Hegner, E., Armstrong, R., Dolgopolova, A., et al. (2014). Reassessment of continental growth during the accretionary history of the Central Asian Orogenic Belt. *Gondwana Research*, *25*(1), 103–125. https://doi.org/10.1016/j.gr.2012.12.023

Kröner, A., Lehmann, J., Schulmann, K., Demoux, A., Lexa, O., Tomurhuu, D., et al. (2010). Lithostratigraphic and geochronological constraints on the evolution of the Central Asian Orogenic Belt in SW Mongolia: Early Paleozoic rifting followed by late Paleozoic accretion. *American Journal of Science*, *310*(7), 523–574. https://doi.org/10.2475/07.2010.01

Kuibida, M. L., Safonova, I. Y., Yermolov, P. V., Vladimirov, A. G., Kruk, N. N., & Yamamoto, S. (2016). Tonalites and plagiogranites of the Char suture-shear zone in East Kazakhstan: Implications for the Kazakhstan-Siberia collision. *Geoscience Frontiers*, *7*(1), 141–150. https://doi.org/10.1016/j.gsf.2015.09.002

Lehmann, J., Schulmann, K., Lexa, O., Corsini, M., Kröner, A., Štípská, P., et al. (2010). Structural constraints on the evolution of the Central Asian Orogenic Belt in SW Mongolia. *American Journal of Science*, *310*(7), 575–628. https://doi.org/10.2475/07.2010.02

Lexa, O., Cosgrove, J., & Schulmann, K. (2004). Apparent shear-band geometry resulting from oblique fold sections. *Journal of Structural Geology*, *26*(1), 155–161. https://doi.org/10.1016/s0191-8141(03)00072-5

Li, H., Li, Y., Xu, X., Yang, G., Wang, Z., Xu, Q., & Ning, W. (2020). Geochemistry, petrogenesis and geological significance of early Carboniferous adakite in Sawuer region, West Junggar, Xinjiang. *Acta Petrologica Sinica*, *36*(7), 2017–2034. https://doi.org/10.18654/1000-0569/2020.07.06

Li, P., Sun, M., Rosenbaum, G., Jourdan, F., Li, S., & Cai, K. (2017). Late Paleozoic closure of the Ob-Zaisan Ocean along the Irtysh shear zone (NW China): Implications for arc amalgamation and oroclinal bending in the Central Asian orogenic belt. *Geological Society of America Bulletin*, *129*(5-6), 547–569. https://doi.org/10.1130/b31541.1

Li, P., Sun, M., Rosenbaum, G., Yuan, C., Safonova, I., Cai, K., et al. (2018). Geometry, kinematics and tectonic models of the Kazakhstan Orocline Central Asian Orogenic Belt. *Journal of Asian Earth Sciences*, *153*, 42–56. https://doi.org/10.1016/j.jseaes.2017.07.029

Liu, B., Han, B.-F., Chen, J.-F., Ren, R., Zheng, B., Wang, Z.-Z., & Feng, L.-X. (2017). Closure time of the Junggar Balkhash Ocean: Constraints from late Paleozoic volcano-sedimentary sequences in the Barleik Mountains, West Junggar, NW China. *Tectonics*, *36*(12), 2823–2845. https://doi.org/10.1002/2017TC004606

Liu, B., Han, B. F., Xu, Z., Ren, R., Zhang, J. R., Zhou, J., et al. (2016). The Cambrian initiation of intra-oceanic subduction in the southern Paleo-Asian Ocean: Further evidence from the Barleik subduction-related metamorphic complex in the West Junggar region, NW China. *Journal of Asian Earth Sciences*, *123*, 1–21. https://doi.org/10.1016/j.jseaes.2016.03.015

Liu, G., She, J., Yang, W., Wang, Q., Jia, J., & Xiao, X. (2018). Zircon U-Pb chronology and geochemistry of the Kalagang Formation volcanic rocks in Bayindala area,West Junggar, and their geological significance (in Chinese with English abstract). *Geology in China*, *45*, 1241–1250. https://doi.org/10.12029/gc20180613

Maus, S., Barckhausen, U., Berkenbosch, H., Bournas, N., Brozena, J., Childers, V., et al. (2009). EMAG2: A 2–arc min resolution Earth magnetic anomaly grid compiled from satellite, airborne, and marine magnetic measurements. *Geochemistry, Geophysics, Geosystems*, *10*(8), 1–12. https://doi.org/10.1029/2009GC002471

Miller, H. G., & Singh, V. (1994). Potential field tilt—A new concept for location of potential field sources. *Journal of Applied Geophysics*, *32*(2–3), 213–217. https://doi.org/10.1016/0926-9851(94)90022-1

Pavlis, N. K., Holmes, S. A., Kenyon, S. C., & Factor, J. K. (2012). The development and evaluation of the Earth Gravitational Model 2008 (EGM2008). *Journal of Geophysical Research*, *117*(B4), 1–38. https://doi.org/10.1029/2011JB008916

Ramsay, J. G. (1967). *Folding and fracturing of rocks* (p. 568). McGraw-Hill.

Schulmann, K., Edel, J. B., Lexa, O., Xiao, W., Třebínová, D., Spikings, R., et al. (2022). Paleomagnetic, tectonic and geochronological constraints for Permian-Triassic oroclinal bending of the Mongolian collage. *National Science Review*, *10*(2). https://doi.org/10.1093/nsr/nwac184/6679568

Schulmann, K., & Paterson, S. (2011). Asian continental growth. *Nature Geoscience*, *4*(12), 827–829. https://doi.org/10.1038/ngeo1339–829

Şengör, A. M. C., & Natal'in, B. A. (1996). Turkic-type orogeny and its role in the making of the continental crust. *Annual Review of Earth and Planetary Sciences*, *24*(1), 263–337. https://doi.org/10.1146/annurev.earth.24.1.263

Şengör, A. M. C., Natalin, B. A., & Burtman, V. S. (1993). Evolution of the Altaid tectonic collage and Paleozoic crustal growth in Eurasia. *Nature*, *364*(6435), 299–307. https://doi.org/10.1038/364299a0

Şengör, A. M. C., Natal'in, B. A., Sunal, G., & van der Voo, R. (2018). The tectonics of the Altaids: Crustal growth during the construction of the continental lithosphere of Central Asia between~750 and~130 Ma ago. *Annual Review of Earth and Planetary Sciences*, *46*(1), 439–494. https://doi.org/10.1146/annurev-earth-060313-054826

Shen, P., Pan, H., Xiao, W., & Shen, Y. (2013). An Ordovician intra-oceanic subduction system influenced by ridge subduction in the West Junggar, Northwest China. *International Geology Review*, *56*(2), 206–223. https://doi.org/10.1080/00206814.2013.839096

Shu, T., Jiang, Y., Schulmann, K., Yu, Y., Yuan, C., Wang, S., et al. (2022). Structure, geochronology, and petrogenesis of Permian peraluminous granite dykes in the southern Chinese Altai as indicators of Altai–East Junggar convergence. *GSA Bulletin*. https://doi.org/10.1130/b36408.1

Soldner, J., Oliot, E., Schulmann, K., Štípská, P., Kusbach, V., & Anczkiewicz, R. (2017). Metamorphic P–T–t–d evolution of (U)HP metabasites from the South Tianshan accretionary complex (NW China)—Implications for rock deformation during exhumation in a subduction channel. *Gondwana Research*, *47*, 161–187. https://doi.org/10.1016/j.gr.2016.07.007

Song, S., Xiao, W., Windley, B. F., Collins, A. S., Chen, Y., Zhang, J., et al. (2020). Late Paleozoic Chingiz and Saur Arc Amalgamation in West Junggar (NW China): Implications for accretionary tectonics in the Southern Altaids. *Tectonics*, *39*(7), e2019TC005781. https://doi.org/10.1029/2019TC005781

Tong, Y., Wang, T., Jahn, B. m., Sun, M., Hong, D. W., & Gao, J. F. (2014). Post-accretionary permian granitoids in the Chinese Altai orogen: Geochronology, petrogenesis and tectonic implications. *American Journal of Science*, *314*(1), 80–109. https://doi.org/10.2475/01.2014.03

Vallée, M. A., Keating, P., Smith, R. S., & St-Hilaire, C. (2004). Estimating depth and model type using the continuous wavelet transform of magnetic data. *Geophysics*, *69*(1), 191–199. https://doi.org/10.1190/1.1649387

Verduzco, B., Fairhead, J. D., Green, C. M., & MacKenzie, C. (2004). New insights into magnetic derivatives for structural mapping. *The Leading Edge*, *23*(2), 116–119. https://doi.org/10.1190/1.1651454

Wang, Y. W., Wang, J. B., Wang, L. J., Long, L. L., Tang, P. Z., Liao, Z., et al. (2012). The Tuerkubantao ophiolite mélange in Xinjiang, NW China: New evidence for the Erqis suture zone. *Geoscience Frontiers*, *3*(5), 587–602. https://doi.org/10.1016/j.gsf.2012.02.002

Whitney, D. L., & Evans, B. W. (2010). Abbreviations for names of rock-forming minerals. *American Mineralogist*, *95*(1), 185–187. https://doi.org/10.2138/am.2010.3371

Wilhem, C., Windley, B. F., & Stampfli, G. M. (2012). The Altaids of Central Asia: A tectonic and evolutionary innovative review. *Earth-Science Reviews*, *113*(3-4), 303–341. https://doi.org/10.1016/j.earscirev.2012.04.001

Windley, B. F., Alexeiev, D., Xiao, W. J., Kroner, A., & Badarch, G. (2007). Tectonic models for accretion of the Central Asian Orogenic Belt. *Journal of the Geological Society*, *164*(1), 31–47. https://doi.org/10.1144/0016-76492006-022

Windley, B. F., Kröner, A., Guo, J. H., Qu, G. S., Li, Y. Y., & Zhang, C. (2002). Neoproterozoic to Paleozoic geology of the Altai orogen, NW China: New zircon age data and tectonic evolution. *The Journal of Geology*, *110*(6), 719–737. https://doi.org/10.1086/342866

Xiao, W., Han, C., Yuan, C., Sun, M., Lin, S., Chen, H., et al. (2008). Middle Cambrian to Permian subduction-related accretionary orogenesis of Northern Xinjiang, NW China: Implications for the tectonic evolution of central Asia. *Journal of Asian Earth Sciences*, *32*(2–4), 102–117. https://doi.org/10.1016/j.jseaes.2007.10.008

Xiao, W., Huang, B., Han, C., Sun, S., & Li, J. (2010). A review of the western part of the Altaids: A key to understanding the architecture of accretionary orogens. *Gondwana Research*, *18*(2–3), 253–273. https://doi.org/10.1016/j.gr.2010.01.007

Xiao, W., Kusky, T., Safonova, I., Seltmann, R., & Sun, M. (2015). Tectonics of the Central Asian Orogenic Belt and its Pacific analogues. *Journal of Asian Earth Sciences*, *113*, 1–6. https://doi.org/10.1016/j.jseaes.2015.06.032

Xiao, W., Windley, B. F., Han, C., Liu, W., Wan, B., Zhang, J., et al. (2018). Late Paleozoic to early Triassic multiple roll-back and oroclinal bending of the Mongolia collage in Central Asia. *Earth-Science Reviews*, *186*, 94–128. https://doi.org/10.1016/j.earscirev.2017.09.020

Xu, Z., Han, B.-F., Ren, R., Zhou, Y.-Z., & Su, L. (2013). Palaeozoic multiphase magmatism at Barleik Mountain, southern West Junggar, Northwest China: Implications for tectonic evolution of the West Junggar. *International Geology Review*, *55*(5), 633–656. https://doi.org/10.1080/00206814.2012.741315

Xu, Z., Han, B.-F., Ren, R., Zhou, Y.-Z., Zhang, L., Chen, J.-F., et al. (2012). Ultramafic–mafic mélange, island arc and post-collisional intrusions in the Mayile mountain, West Junggar, China: Implications for Paleozoic intra-oceanic subduction–accretion process. *Lithos*, *132–133*, 141–161. https://doi.org/10.1016/j.lithos.2011.11.016

Yang, G., Li, Y., Gu, P., Yang, B., Tong, L., & Zhang, H. (2012). Geochronological and geochemical study of the Darbut Ophiolitic Complex in the West Junggar (NW China): Implications for petrogenesis and tectonic evolution. *Gondwana Research*, *21*(4), 1037–1049. https://doi.org/10.1016/j.gr.2011.07.029

Yang, G., Li, Y., Santosh, M., Xiao, W., Yang, B., Tong, L., & Zhang, S. (2015). Alkaline basalts in the Karamay ophiolitic mélange, NW China: A geological, geochemical and geochronological study and implications for geodynamic setting. *Journal of Asian Earth Sciences*, *113*, 110–125. https://doi.org/10.1016/j.jseaes.2014.08.017

Yang, G., Li, Y., Santosh, M., Yang, B., Zhang, B., & Tong, L. (2013). Geochronology and geochemistry of basalts from the Karamay ophiolitic melange in West Junggar (NW China): Implications for Devonian-Carboniferous intra-oceanic accretionary tectonics of the southern Altaids. *Geological Society of America Bulletin*, *125*(3–4), 401–419. https://doi.org/10.1130/b30650.1

Yang, G., Li, Y., Tong, L., Wang, Z., & Si, G. (2020). An Early Cambrian plume-induced subduction initiation event within the Junggar Ocean: Insights from ophiolitic mélanges, arc magmatism, and metamorphic rocks. *Gondwana Research*, *88*, 45–66. https://doi.org/10.1016/j.gr.2020.07.002

Yang, Y., Zhao, L., Xu, Q., Zheng, R., Liu, J., & Zhang, J. (2019). Early Paleozoic tectonic evolution of the northern West Junggar (NW China): Constraints from early Cambrian–middle Silurian felsic plutons of the Chagantaolegai ophiolitic mélange. *Lithos*, *350–351*, 105225. https://doi.org/10.1016/j.lithos.2019.105225

Yang, Y., Zhao, L., Zhang, J., & Niu, M. (2021). Middle Paleozoic archipelago amalgamation and tectonic transform in the northern West Junggar, NW China: Constraints from magmatism and deformation. *Gondwana Research*, *98*, 147–165. https://doi.org/10.1016/j.gr.2021.04.010

Yang, Y., Zhao, L., Zheng, R., & Xu, Q. (2019). Evolution of the early Paleozoic Hongguleleng–Balkybey Ocean: Evidence from the Hebukesaier ophiolitic mélange in the northern West Junggar, NW China. *Lithos*, *324–325*, 519–536. https://doi.org/10.1016/j.lithos.2018.11.029

Yang, Y., Zhao, L., Zheng, R., Xu, Q., Liu, J., & Zhang, J. (2020). An early Ordovician fossil seamount of the Hongguleleng–Balkybey Ocean in the northern West Junggar terrane (NW China) and its implications for the ocean evolution. *Journal of Asian Earth Sciences*, *194*, 104066. https://doi.org/10.1016/j.jseaes.2019.104066

Yin, J., Long, X., Yuan, C., Sun, M., Zhao, G., & Geng, H. (2013). A late Carboniferous–early Permian slab window in the West Junggar of NW China: Geochronological and geochemical evidence from mafic to intermediate dikes. *Lithos*, *175–176*, 146–162. https://doi.org/10.1016/j.lithos.2013.04.005

Zhang, C., Santosh, M., Liu, L., Luo, Q., Zhang, X., & Liu, D. (2018a). Early Silurian to Early Carboniferous ridge subduction in NW Junggar: Evidence from geochronological, geochemical, and Sr-Nd-Hf isotopic data on alkali granites and adakites. *Lithos*, *300–301*, 314–329. https://doi.org/10.1016/j.lithos.2017.12.010

Zhang, C. L., Santosh, M., Zou, H. B., Xu, Y. G., Zhou, G., Dong, Y. G., et al. (2012). Revisiting the "Irtish tectonic belt": Implications for the Paleozoic tectonic evolution of the Altai orogen. *Journal of Asian Earth Sciences*, *52*, 117–133. https://doi.org/10.1016/j.jseaes.2012.02.016

Zhang, J. E., Xiao, W. J., Han, C. M., Ao, S. J., Yuan, C., Sun, M., et al. (2011). Kinematics and age constraints of deformation in a Late Carboniferous accretionary complex in Western Junggar, NW China. *Gondwana Research*, *19*(4), 958–974. https://doi.org/10.1016/j.gr.2010.10.003

Zhang, P., Wang, G., Polat, A., Zhu, C., Shen, T., Chen, Y., et al. (2018b). Emplacement of the ophiolitic mélanges in the west Karamay area: Implications for the late Paleozoic tectonic evolution of West Junggar, northwestern China. *Tectonophysics*, *747–748*, 259–280. https://doi.org/10.1016/j.tecto.2018.08.019

Zhang, P., Wang, G., Shen, T., & Zhu, C. (2019). Late Paleozoic back-arc basin in West Junggar (northwestern China): New geochronological and petrogenetic constraints from basalts and cherts in the western Karamay area. *Journal of Geodynamics*, *126*, 1–11. https://doi.org/10.1016/j.jog.2019.03.002

Zhang, P., Wang, G., Polat, A., Shen, T., Chen, Y., Zhu, C., & Wu, G. (2018c). Geochemistry of mafic rocks and cherts in the Darbut and Karamay ophiolitic mélanges in West Junggar, northwestern China: Evidence for a Late Silurian to Devonian back-arc basin system. *Tectonophysics*, *745*, 395–411. https://doi.org/10.1016/j.tecto.2018.08.018

Zhang, Y., & Guo, Z. (2010). New constrains on formation ages of ophiolites in northern Junggar and ccomparative study on their connection. *Acta Petrologica Sinica*, *26*, 421–430.

Zheng, B., Han, B.-F., Liu, B., & Wang, Z. Z. (2019). Ediacaran to Paleozoic magmatism in West Junggar Orogenic Belt, NW China, and implications for evolution of Central Asian Orogenic Belt. *Lithos*, *338–339*, 111–127. https://doi.org/10.1016/j.lithos.2019.04.017

Zheng, B., Han, B. F., Wang, Z. Z., Liu, B., & Feng, L. X. (2020). An example of phanerozoic continental crustal growth: The West Junggar Orogenic Belt, Northwest China. *Lithos*, *376–377*, 105745. https://doi.org/10.1016/j.lithos.2020.105745

Zhou, T., Yuan, F., Fan, Y., Zhang, D., Cooke, D., & Zhao, G. (2008). Granites in the Sawuer region of the west Junggar, Xinjiang Province, China: Geochronological and geochemical characteristics and their geodynamic significance. *Lithos*, *106*(3–4), 191–206. https://doi.org/10.1016/j.lithos.2008.06.014

References From the Supporting Information

Li, X., Tang, G., Gong, B., Yang, Y., Hou, K., Hu, Z., et al. (2013). Qinghu zircon: A working reference for microbeam analysis of U-Pb age and Hf and O isotopes. *Chinese Science Bulletin*, *58*(36), 4647–4654. https://doi.org/10.1007/s11434-013-5932-x

Ludwig, K. R. (2012). Isoplot/Ex Version 4.15. *A Geochronological Toolkit for Microsoft Excel* (Vol. 5, p. 75). Berkeley Geochronology Center Special Publication. Retrieved from https://www.bgc.org/isoplot

Pearce, N. J. G., Perkins, W. T., Westgate, J. A., Gorton, M. P., Jackson, S. E., Neal, C. R., & Chenery, S. P. (1997). A compilation of new and published major and trace element data for NIST SRM 610 and NIST SRM 612 glass reference materials. *Geostandards and Geoanalytical Research*, *21*(1), 115–144. https://doi.org/10.1111/j.1751-908X.1997.tb00538.x

Sláma, J., Košler, J., Condon, D. J., Crowley, J. L., Gerdes, A., Hanchar, J. M., et al. (2008). Plešovice zircon—A new natural reference material for U–Pb and Hf isotopic microanalysis. *Chemical Geology*, *249*(1–2), 1–35. https://doi.org/10.1016/j.chemgeo.2007.11.005